# Regulation of adaptive growth decisions via phosphorylation of the TRAPPII complex in Arabidopsis.

Christian Wiese[1,2], Miriam Abele[2,3], Benjamin Al[2], Melina Altmann[4], Alexander Steiner[2], Nils Kalbfuß[2], Alexander Strohmayr[1,2], Raksha Ravikumar[2], Chan Ho Park[5], Barbara Brunschweiger[2], Chen Meng[3], Eva Facher[6], David W. Ehrhardt[5], Pascal Falter-Braun[4], Zhi-Yong Wang[5], Christina Ludwig[3] and Farhah F. Assaad[1,2,*]

[1]Biotechnology of Natural Products, TUM School of Life Sciences, Technical University of Munich, 85354 Freising, Germany.
[2]Botany, TUM School of Life Sciences, Technical University of Munich, 85354 Freising, Germany.
[3]Bavarian Center for Biomolecular Mass Spectrometry (BayBioMS), TUM School of Life Sciences, Technical University of Munich, 85354 Freising, Germany.
[4]Institute of Network Biology (INET), Helmholtz Center Munich, German Research Center for Environmental Health, 85764 Neuherberg, Germany.
[5]Department of Plant Biology, Carnegie Institution for Science, Stanford, 94305 California, USA.
[6]Systematic Botany and Mycology, Faculty of Biology, Ludwig-Maximilians-Universität (LMU) München, 82152 Planegg-Martinsried, Germany.
* Corresponding author. Email: farhah.assaad@tum.de

## ABSTRACT

Plants often adapt to adverse or stress conditions via differential growth. The trans-Golgi Network (TGN) has been implicated in stress responses, but it is not clear in what capacity it mediates adaptive growth decisions. In this study, we assess the role of the TGN in stress responses by exploring the interactome of the Transport Protein Particle II (TRAPPII) complex, required for TGN structure and function. We identified physical and genetic interactions between TRAPPII and shaggy-like kinases (GSK3/AtSKs). Kinase assays and pharmacological inhibition provided *in vitro* and *in vivo* evidence that AtSKs target the TRAPPII-specific subunit AtTRS120/TRAPPC9. GSK3/AtSK phosphorylation sites in AtTRS120/TRAPPC9 were mutated, and the resulting AtTRS120 phosphovariants subjected to a variety of single and multiple stress conditions *in planta*. The non-phosphorylatable TRS120 mutant exhibited enhanced adaptation to multiple stress conditions and to osmotic stress whereas the phosphomimetic version was less resilient.

Higher order inducible *trappii atsk* mutants had a synthetically enhanced defect in root gravitropism. Our results suggest that the TRAPPII phosphostatus mediates adaptive responses to abiotic cues. AtSKs are multifunctional kinases that integrate a broad range of signals. Similarly, the TRAPPII interactome is vast and considerably enriched in signaling components. An AtSK-TRAPPII interaction would integrate all levels of cellular organization and instruct the TGN, a central and highly discriminate cellular hub, as to how to mobilize and allocate resources to optimize growth and survival under limiting or adverse conditions.

**Key words:** TRAPPII, GSK3/shaggy-like kinases, BRASSINOSTEROID INSENSITIVE 2 (BIN2), decision-making, growth trade-offs, light responses, water stress, adaptation, osmotic stress, additive stress, gravitropism, TGN, Arabidopsis

## INTRODUCTION

Plant responses to environmental stimuli involve diverse forms of growth or movement. The slow, cyclic movement of shoots and stems helps climbing plants such as vines find supportive structures, and stem growth or tendrils are then used to wrap around and cling to such structures (Darwin, 1880). Leaf movements linked to the circadian rhythm enable plants to maximize their exposure to sunlight (McClung, 2006). Tropisms are additional examples of movement in plants: the shoot bends towards directional light, whereas the root bends away from the light. In addition to phototropism, plants have tropic responses to a range of stimuli including moisture, fluctuations in temperature, gravity, touch and other mechanical cues (Garzón & Keijzer, 2011). Darwin argues that the movements of plants are driven by growth and the need to access resources, such as sunlight and water (Darwin, 1880). Gyrations, revolutions and tropisms require some form of differential growth or bending at the organ level. Bending is achieved when one side of an organ grows more rapidly than the opposing side. This differential growth is a result, at least in part, of the differential sorting of PIN-FORMED (PIN) auxin transporters, resulting in the unequal distribution of auxin, a morphogen, at opposing sides of a cell (Friml *et al*, 2002; Ding *et al*, 2011). It follows that differential growth responses such as bending require differential sorting decisions. How environmental stimuli are translated into sorting decisions remains largely unclear.

The sorting of PIN transporters has been shown to require trans-Golgi network (TGN) function. Indeed, disruption of TGN function by mutation results in the ectopic distribution of PIN or AUX proteins (Naramoto *et al*, 2014; Qi *et al*, 2011; Rybak *et al*, 2014; Ravikumar *et al*, 2018). The

TGN plays a key role not only in the sorting of macromolecules, but also in exocytosis and endocytosis. In addition, the TGN performs specialized functions such as cytokinesis, cell differentiation, the establishment of cell polarity, and anisotropic growth (Gendre *et al*, 2015; Ravikumar *et al*, 2017). As an early endosome, the plant TGN is a central hub in the flow of information to and from the plant cell surface (Uemura, 2016). The plant TGN has been implicated in responses to abiotic stimuli such as drought, heat, salt stress and osmotic stress and to biotic stimuli such as fungal attack (Rosquete & Drakakaki, 2018). Studies on the role of the TGN in stress responses have been carried out predominantly with core trafficking components such as Rab GTPases, tethering factors, and Q-SNAREs, required for membrane tethering, docking and fusion (Rosquete & Drakakaki, 2018; Ravikumar *et al*, 2017). Trafficking mutants typically exhibit root growth defects and/or hypersensitivity to abiotic cues such as salt stress, osmotic stress, drought or heat (Asaoka *et al*, 2013; Kim & Bassham, 2011; Lee *et al*, 2006; Rosquete *et al*, 2019; Uemura *et al*, 2012; Wang *et al*, 2011; Zhu *et al*, 2002). However, whether trafficking mutants have primary defects in growth with secondary consequences in stress responses, or whether the primary defects lie in an impaired response to stress factors remains unclear. More broadly, in the context of stress responses the question pertains as to whether the TGN is involved in decision-making processes *per se*, or merely in the execution of adaptive growth decisions.

As regards decision-making processes, there is a growing body of evidence to suggest that plants have the ability to learn, to process information, to communicate, to reach decisions, and in general to exhibit behavior that could be considered cognitive (reviewed in Severino, 2021). Severino (2021) makes the case for experimental approaches to study the decisions plant reach in complex environments. A recent experimental approach for the study of decision-making processes in germinating seedlings has incorporated two tools used in decision theory: the use of a limited budget and of conflict-of interest scenarios (Kalbfuß *et al*, 2022). A limited budget was achieved by germination in the dark in the absence of a carbon source, such that the only available energy source is that available in the seed (Kalbfuß *et al*, 2022). A conflict-of-interest scenario comprises the simultaneous withdrawal of light, which promotes hypocotyl elongation, and water, which promotes root elongation (Kalbfuß *et al*, 2022). As the severity of water stress increased, root length increased while hypocotyl length decreased; importantly, the total seedling length remained constant (Kalbfuß *et al*, 2022). Thus, trade-offs in hypocotyl versus root growth were observed and these comprise a binary readout for responses to these additive stress conditions. Decision mutants were defined as mutants that were either incapable of adjusting their hypocotyl/root ratios in response to additive stress, or that consistently reached the wrong growth

103 decisions as compared to the wild type (Kalbfuß *et al*, 2022). By emphasizing growth trade-offs,
104 the experimental approach developed by Kalbfuß *et al* (2022) is aligned with the definition of
105 decision-making as entailing an appraisal of the advantages and disadvantages of various
106 courses of action (Karban & Orrock, 2018). While Kalbfuß *et al* (2022) address decision-making
107 at a cellular level, the literature on plant decision-making has, to our knowledge, not included
108 considerations about the possible role of the TGN.
109
110 To understand the role of the TGN in adaptive or stress responses, it would be important to deploy
111 a battery of gene products not only broadly associated with or localized to the TGN, but also
112 intrinsic to TGN structure and function. Two such proteins or complexes are ECHIDNA and the
113 Transport Protein Particle II (TRAPPII) complex. ECHIDNA was identified as an upregulated
114 transcript in elongating cells (Gendre *et al*, 2011). Yeast and metazoan TRAPPII is a hetero-
115 oligomeric complex that acts as a Guanine nucleotide Exchange Factor (GEF) for Rab GTPases,
116 converting GDP-bound inactive Rab GTPases to active GTP-bound forms (Cai *et al*, 2005;
117 Morozova *et al*, 2006; Pinar *et al*, 2015; Thomas & Fromme, 2016; Riedel *et al*, 2018). TRAPPII
118 has been shown to play a key role in the regulation of the TGN in all eukaryotes, but our
119 understanding of its potential physiological roles is incomplete (Pinar & Peñalva, 2020). The
120 Arabidopsis TRAPPII (AtTRAPPII) complex was identified by mutation in screens for seedlings
121 with aberrant morphogenesis or cytokinesis defects (Söllner *et al*, 2002; Thellmann *et al*, 2010;
122 Jaber *et al*, 2010). AtTRAPPII most resembles fungal and metazoan TRAPPII complexes, with
123 the exception of one plant-specific subunit (Garcia *et al*, 2020; Kalde *et al*, 2019; Pinar *et al*, 2019).
124 We have previously shown that ECHIDNA and TRAPPII have overlapping yet distinct functions at
125 the TGN in Arabidopsis (Ravikumar *et al*, 2018). ECHIDNA is primarily required for the genesis of
126 secretory vesicles and, as a consequence, for cell expansion (Boutté *et al*, 2013; Gendre *et al*,
127 2013; McFarlane *et al*, 2013). AtTRAPPII plays a role not only in basal TGN functions - exocytosis,
128 endocytosis, protein sorting - but also in more specialized TGN functions such as cytokinesis and
129 the establishment of cell polarity (Ravikumar *et al*, 2018). Whether or not AtTRAPPII plays a role
130 in responses to abiotic cues such as osmotic or drought stress remains to be determined.
131
132 In this study, we focus on the TRAPPII complex as a starting point as it is required for all aspects
133 of TGN function, including the sorting of proteins such as PINs to distinct membrane domains (Qi
134 *et al*, 2011; Rybak *et al*, 2014; Ravikumar *et al*, 2018). We first explored the TRAPPII interactome
135 and also surveyed dynamic or conditional interactions. Together with yeast two-hybrid screens,
136 this identified shaggy-like kinases such as AtSK21/BIN2 as TRAPPII interactors. We corroborated

137 this finding with *in vitro* kinases assays and pharmacological inhibition *in vivo*. Shaggy-like kinases
138 are multi-taskers that integrate a vast number of biotic and abiotic cues (Lv & Li, 2020; Planas-
139 Riverola *et al*, 2019; Youn & Kim, 2015; Li *et al*, 2021; Song *et al*, 2023). AtSK21/BIN2 has recently
140 been implicated in decision-making in the Arabidopsis seedling (Kalbfuß *et al*, 2022). We explore
141 the meaning of the AtSK-TRAPPII interaction using a variety of assays to monitor stress
142 responses and differential growth decisions.
143
144
145 **RESULTS**
146 **The TRAPPII interactome contains a large number of signaling components**
147 To gain insight into TGN function, we used the TRAPPII interactome as a starting point. We have
148 previously identified TRAPP and EXOCYST subunits, cytoskeletal proteins and Rab GTPases in
149 the TRAPPII interactome (Rybak *et al*, 2014; Steiner *et al*, 2016; Kalde *et al*, 2019; Garcia *et al*,
150 2020). However, no global meta-analysis of the vast Arabidopsis TRAPPII interactome has been
151 carried out to date. We, therefore, performed a gene ontology (GO) term enrichment analysis.
152 AtTRAPPII consists of seven shared core subunits and three TRAPPII-specific subunits
153 (AtTRS120/TRAPPC9, CLUB/AtTRS130/TRAPPC10 and TRIPP; Garcia *et al*, 2020; Kalde *et al*,
154 2019). We focused on the TRAPPII-specific CLUB:GFP interactome. This interactome was
155 significantly enriched (fold-enrichment ≥ 4; adjusted *P*-value ≤ 0.003) in proteins involved in cell
156 division and in trafficking or transport (Fig. 1A; Fig. S1A), which is consistent with known
157 cytokinesis, trafficking, sorting and TGN defects in *trappii* mutants (Jaber *et al*, 2010; Qi *et al*,
158 2011; Rybak *et al*, 2014; Ravikumar *et al*, 2018). GO terms describing root hair elongation and
159 microtubule organization were also scored (Fig. 1A), and this is equally unsurprising in light of
160 *trappii* defects in root hair tip growth and microtuble organization (Jaber *et al*, 2010; Söllner *et al*,
161 2002; Thellmann *et al*, 2010; Steiner *et al*, 2016). Interestingly, a large number of significantly
162 enriched GO categories describe responses to stimuli such as light, metal ions or sugar (grouped
163 under “signaling”, “response to stimulus”, “light responses” or “photosynthesis” in Fig. 1A and Fig.
164 S1A). The large number of enriched GO terms implicated in signaling suggests that AtTRAPPII
165 may act as a cellular hub.
166 To further explore a possible implication of the TRAPPII complex in signaling, we surveyed the
167 dynamic interactome, by which we refer to interactors perceived under one environmental
168 condition (for example in the light) but not in another (for example in the dark). By these criteria,
169 brassinosteroid (BR) signaling components were significantly enriched (P = 0.016); this category
170 encompasses 11 proteins, of which 9 were detected in CLUB:GFP immunoprecipitates from light-

171 grown influorescences (Fig. 1B-C; Fig. S1B; Table S2). Among these were the TOR kinase and a
172 family of shaggy-like kinases (AtSKs; Fig. 1C; Fig. S1B; Table S2). TOR signaling was also a
173 significantly enriched GO term in the TRAPPII interactome (Fig. 1A). TOR and AtSKs are highly
174 significant interactors in the TRAPPII-specific subunit CLUB:GFP interactome (Fig. 1B-C; Fig.
175 S1B). They show a fold change that is lower than seen for components of the TRAPPII complex,
176 but similar to that seen for validated interactors such as RAB-A2a and MAP65, expected to form
177 more transient associations (Fig. 1B-C; Kalde *et al*, 2019; Steiner *et al*, 2016). We then used yeast
178 two-hybrid (Y2H) to probe for binary interactions between TRAPPII and signaling components
179 identified in the IP-MS. Y2H was carried out with TRAPPII subunits and truncations thereof (Fig.
180 2A; Kalde *et al*, 2019; Steiner *et al*, 2016; Garcia *et al*, 2020). In a large scale Y2H screen including
181 2400 pair-wise tests, an interaction was detected between a TRS120$^{499-1187}$ truncation (TRS120-
182 T2) and the shaggy-like kinase BIN2 (AtSK21; Fig. 2B). BIN2 interacted specifically with
183 AtTRS120 and not with other tested TRAPPII subunits (Fig. 2B). Furthermore, we did not detect
184 any other TRAPPII-kinase interactions in our pairwise Y2H assays. In conclusion, mass
185 spectrometry and Y2H identify physical interactions between TRAPPII and AtSKs, *in planta* and
186 in a heterologous system.
187
188 **The TRAPPII complex is a target of shaggy-like kinases**
189 To assess whether the TRAPPII complex is a target of AtSK/GSK3 kinases, we first looked for the
190 presence of phosphopeptides in co-immunoprecipitates. To this end, we immunoprecipitated two
191 TRAPPII-specific subunits, AtTRS120 and CLUB/AtTRS130, and looked for phosphopeptides via
192 mass spectrometry. This provided ample *in vivo* evidence for TRAPPII AtTRS120 phosphorylation
193 at AtSK/GSK3 sites (Fig. S2). Furthermore, shaggy-like kinases were detected in IP-MS not only
194 with the TRAPPII-specific subunit CLUB/AtTRS130 (Fig. 1B-C; Fig. S1B) but also with the
195 TRAPPII-specific subunit AtTRS120 (Fig. S3). The Arabidopsis genome encodes ten shaggy-like
196 kinases (AtSKs), which are classified into four clades (Fig. S3A). Razor peptides covering all four
197 clades were found in the AtTRS120:GFP interactome (Fig. S3B-D).
198 The TRS120-T2 truncation contains the GSK3 sites we had found to be phosphorylated *in vivo*
199 (Fig. S2; see yellow highlights in Fig. 2C). Our nomenclature for these sites is α, β and γ, which is
200 short for TRS120-S922:S923 (α), TRS120-S971:S973:S974:S975 (β) and TRS120-S1165 (γ; Fig.
201 2C). These reside in the plant-specific moiety of AtTRS120 and are embedded in plant-specific
202 sequences (see green shading in Fig. 2A; Fig. 2D) at the dimer interface inferred from extensive
203 pair-wise Y2H tests in Arabidopsis (Kalde *et al*, 2019; Garcia *et al*, 2020) and consistent with cryo-
204 electron micrograph (cryo-EM) structures of yeast and metazoan TRAPPII (Galindo *et al*, 2021;

205 Mi *et al*, 2022; Bagde & Fromme, 2022). AlphaFold structural predictions (Varadi *et al*, 2022;
206 Jumper *et al*, 2021) show that the three sites reside in unstructured, flexible and accessible regions
207 of the AtTRS120 protein, as is observed in the majority of modified amino acid residues (Fig. 2E;
208 Jiménez *et al*, 2007). Furthermore, a cross-kingdom structural alignment of AtTRS120 and
209 CLUB/AtTRS130 with cryo-EM-generated structures of yeast TRAPPII (Mi *et al*, 2022) showed
210 that the β and γ phosphorylation sites face the active site chamber or Rab GTPase binding pocket
211 predicted by Mi *et al* (2022) and Bagde & Fromme (2022) (Fig. S4). To study the three sites, we
212 generated site directed mutations in TRS120-T2, mutating the serine (S) and threonine (T)
213 residues (depicted in red in Fig. 2C) to non-phosphorylatable alanine (A) residues, or to aspartate
214 (D) to mimic constitutive phosphorylation. In the case of the TRS120-Sβ site, for example, we
215 designate these variants as TRS120-SβA or TRS120-SβD (Fig. 2F; Fig. 3A). The point mutations
216 were introduced into cDNA sequences for expression in yeast and bacteria. In Y2H screens, the
217 BIN2-TRS120 interaction, but not TRAPPII complex interactions, was almost abolished when all
218 three sites were phosphomimetic (TRS120-T2 SαβγD; Fig. 2F). As kinases typically have kiss and
219 run interactions with their unphosphorylated substrates, and as BIN2 interacts more strongly with
220 an unphosphorylated than a phosphorylated substrate (Pusch *et al*, 2012; Tang *et al*, 2011), this
221 is consistent with AtTRS120/TRAPPC9 being targeted by the BIN2 kinase.
222
223 The IP-MS and Y2H interactions were validated with *in vitro* kinase assays, performed with a
224 phosphorus radioisotope (Fig. 3A; Fig. S5A). This showed that BIN2 and AtSK11 phosphorylated
225 AtTRS120-T2 *in vitro,* with a preference for wild-type sequences over non-phosphorylatable
226 substrates such as AtTRS120-SαβγA (Fig. 3A; Fig. S5A). Further, the phosphorylation was
227 confirmed with mass-spectrometry using non-radioactive assays. The mass-spectrometry results
228 showed that the AtTRS120 α, β, and γ sites phosphorylated *in vivo* (Fig. S2; IP-MS on seedlings
229 using TRS120:GFP as bait) were phosphorylated by AtSKs *in vitro* (Fig. 3B; Fig. S5B). Kinase
230 assays performed with varying kinase concentrations (but constant substrate concentrations)
231 showed that the phosphorylation events were time and/or concentration dependent (Fig. 3B; Fig.
232 S5B). AtTRS120 was a substrate of AtSKs in clades I-III; we did not detect phosphorylation of
233 AtTRS120 with a clade IV AtSK *in vitro* (Fig. 3B). All AtSKs that targeted AtTRS120 had a marked
234 and consistent preference for the TRS120-γ (S1165) site (Fig. 3B; Fig. S5B). *In vivo*, IP-MS
235 performed on seedlings treated with the AtSK inhibitor bikinin showed a reduced extent of
236 phosphorylation of the TRS120-γ peptide (Fig. S6). Conversely, seedlings treated with the BR
237 biosynthesis inhibitor PPZ, which should relieve BR-mediated BIN2 inhibition, showed an
238 increased extent of phosphorylation of the TRS120-γ peptide (Fig. S6). These *in vivo* observations

239 are consistent with the *in vitro* kinase assays (Fig. 3; Fig. S5). In summary, several lines of *in vitro*
240 (Y2H, kinase assays) and *in vivo* (IP-MS, pharmacological inhibition) evidence support the
241 conclusion that the TRAPPII subunit AtTRS120 is a substrate of shaggy-like kinases.
242
243 **BIN2 and TRAPPII are required for differential growth decisions under additive stress**
244 As TRAPPII is a BIN2 substrate, a question is whether *bin2* and *trappii* mutants have related
245 phenotypes. We were not able to detect cytokinesis or protein sorting defects, characteristic of
246 *trappii,* in semi-dominant *bin2-1* alleles (Fig. S7). We have recently shown that BIN2 is required
247 for hypocotyl versus root trade-offs in the germinating seedling under additive stress conditions
248 involving the simultaneous withdrawal of both light and water (Kalbfuß *et al*, 2022). Water stress
249 in the dark is a "conflict of interest" scenario in which hypocotyl and root growth have competing
250 interests (Kalbfuß *et al*, 2022). Kalbfuß *et al* (2022) defined decision mutants as ones that had
251 either insignificant hypocotyl/root-ratio responses ($P > 0.05$), or consistently wrong growth
252 responses as compared to the wild type ($P < 0.05$ but for an opposite growth phenotype, as
253 depicted by red asterisks in Fig. 4B-D; Kalbfuß *et al*, 2022). Under additive stress, *trappii* null
254 mutants failed to adjust their hypocotyl length along the same line as the wild type (red asterisks
255 in Fig. 4C-D; Fig. 4F; see Fig. S8D-E for a direct comparison to the wild type and for the distribution
256 of datapoints). In particular, *trappii trs120-4* mutants had non-significant hypocotyl/root ratio
257 responses to water withdrawal in the dark (Fig. 4D; Fig. S8E). In addition to comparing organ
258 lengths, each mutant line was normalized to its corresponding wild-type ecotype on the same
259 (PEG) plate, which helped us to take the variability between PEG plates and experiments into
260 account and enabled us to pool biological replicates (see methods for further detail). To this end,
261 the response to water stress in the dark was represented as a normalized response quotient (RQ).
262 The RQ is an indication of how well each mutant responds to a given combination of stress cues
263 and indicates how much each line deviates from the wild type. A value of 1.0 means that the
264 mutant line behaves exactly like its corresponding wild type. This rendition shows that *bin2* higher
265 order and *trappii* null alleles considerably deviated from the wild type, with severely attenuated
266 responses (Fig. 4G; Fig. S9). We reason that decision mutants unable to integrate environmental
267 cues might have highly variable hypocotyl versus root lengths. This high variance would, in turn,
268 translate into an insignificant (i.e. high) *P*-value, indicative of a low signal-to-noise ratio. We,
269 therefore, plotted the median *P*-values against the normalized response quotients (referred to as
270 volcano plots; mean $RQ_{ratio}$ in Fig. 4H). Wild-type ecotypes had significant *P*-values $< 10^{-10}$ (grey
271 shading on the red line in Fig. 4H, green arrow). Mutants with insignificant *P*-values and response
272 quotients considerably smaller than 1.0 would be considered "confused" decision mutants and

273 these would map in the lower left quadrant of the $RQ_{ratio}$ volcano plot (see peach shading in Fig.
274 4H). *bin2* higher order null alleles and *trs120-4* mutants clustered together in the lower left region
275 of the volcano plot (see peach shading in Fig. 4H); both qualify as decision mutants (Fig. 4B, 4D,
276 4G-H; Kalbfuß *et al*, 2022). This was in contrast to the near-wild-type phenotype of higher order
277 null mutants impaired in the perception of light or water stress (*phyAphyBcry1cry2* and
278 *pyr1pyl1pyl2pyl4* in Fig. 4G-H). We conclude that *bin2* higher order and *trappii* null alleles are
279 decision mutants.
280
281 A question that arises is whether *trappii* mutants are impaired in differential growth decisions as a
282 secondary consequence of primary defects in morphogenesis or cytokinesis (Jaber *et al*, 2010;
283 Rybak *et al*, 2014; Thellmann *et al*, 2010). The etiolation response was severely attenuated in
284 *trappii* mutants, but nonetheless highly significant ($P < 0.00001$; Fig. S10C-D, S10F-I). Similarly,
285 an attenuated but clear etiolation response has been shown for other cytokinesis-defective
286 mutants including *keule* and *knolle* (Assaad *et al*, 2001). This shows that, despite a severe
287 impairment in cell division and morphogenesis, cytokinesis-defective mutants are nonetheless
288 capable of differential growth. In addition to their cytokinesis defect, *trappii* mutants are impaired
289 in TGN function (Ravikumar *et al*, 2018). We, therefore, compared *trappii* mutants to *echidna*
290 mutants, severely impaired in TGN structure and function (Boutté *et al*, 2013; Gendre *et al*, 2013;
291 McFarlane *et al*, 2013). Both *echidna* and *trappii* mutants exhibited a severe impairment in root
292 elongation in the light (Fig. S10C-F; Fig. S10H). In contrast to *trappii*, however, *echidna* mutants
293 had highly significant responses to additive stress that resembled the wild type in all respects (Fig.
294 4E-H; Fig. S8F). Thus, *echidna* mutants do not qualify as decision mutants. In conclusion, a
295 comparison to other cytokinesis-defective or TGN mutants suggests that neither cytokinesis
296 defects nor TGN malfunction suffice to explain the *trappii trs120-4* decision phenotype.
297
298 Cellular growth parameters in *trappii* were assessed under single versus additive stress, in both
299 the hypocotyl and root tip. The width, height and surface area of *trappii* hypocotyl cells grown in
300 the light did not show any deviation from the wild type (Fig. 5A-B light; Fig. S11A-D light). In wild-
301 type hypocotyls, both organ length and cell length decreased in response to water stress in the
302 dark (Fig. 4A; Fig. 5A; Fig. S11C). In contrast, in *trappii* mutants, organ and cell length significantly
303 increased (red asterisks or compact letter displays in Fig. 4C-D, Fig. 5B and Fig. S11A, C-D
304 highlight a phenotype consistently opposite to the wild type). This was more pronounced in *trs120-*
305 *4* (1.71-fold increase; Fig. 5B) than in *club-2* (1.46-fold increase; Fig. S11A) whereas the wild-type
306 Col-0 showed a 0.55-fold decrease in cell length (Fig. 5A). In root tips, we monitored meristem

307 properties and cell length along single cortical cell files as a function of distance from the quiescent
308 center. In the wild type, meristem size was large in the light, intermediate in the dark and shortest
309 under water stress in the dark (darkW; Fig. 5C). In contrast, meristem size in *trs120-4* remained
310 constant under the three environmental conditions tested (Fig. 5D). We have recently shown that
311 root growth in response to water stress in the dark is due to a combination of cell division and
312 rapid exit from the meristem (Kalbfuß *et al*, 2022). An early exit from the meristem can be
313 visualized as cell elongation in cells close to the quiescent center. This was observed under dark
314 and darkW conditions in the wild type (green arrows in Fig. 5C) but not in the *trappii* mutant *trs120-*
315 *4* (magenta arrows in Fig. 5D). While the curves differed under the different environmental
316 conditions in the wild type (Fig. 5C), these were fairly similar regardless of the environmental cue
317 in *trs120-4* (magenta arrows in Fig. 5D; note that the grey shading, which designates the 95%
318 confidence interval, overlaps). We conclude that, at a cellular level, *trappii trs120-4* mutants are
319 unable to differentially regulate their growth parameters in response to additive stress (Fig. 5; Fig.
320 S11). This would suffice to explain the growth defects we observed at the organ level (Fig. 4). The
321 *trappii* cellular phenotype in the decision screen is reminiscent of that reported for *bin2* (Kalbfuß
322 *et al*, 2022). In summary, *bin2* and *trappii* alleles have related phenotypes with respect to an
323 inability to differentially regulate cell growth in both the hypocotyl and root tip in response to
324 additive stress (Figs. 4-5; cf. Kalbfuß *et al*, 2022).
325
326 **AtTRS120 phosphovariants are functional**
327 To assess the *in vivo* impact of the TRS120 phosphorylation status on intracellular localization,
328 targeted point mutations at the TRS120 AtSK sites (Fig. 2C) were introduced into genomic
329 sequences capable of rescuing the *trs120-4* mutant phenotype (Rybak *et al*, 2014). The TRS120
330 constructs were fused to a C-terminal GFP tag and we refer to the ensuing site-directed mutants
331 as TRS120 phosphovariants. The constructs were expressed and capable of rescuing the null
332 *trs120-4* allele in the T1 and T2 generations (Fig. S12A-B); upon further propagation, however,
333 signs of silencing were evident in seedlings (Fig. S12C-D). The wild-type TRAPPII complex
334 resides in the cytosol, at the TGN and at the cell plate (Fig. S13; Naramoto *et al*, 2014; Qi *et al*,
335 2011; Ravikumar *et al*, 2018; Rybak *et al*, 2014). Phosphovariants had a similar appearance, but
336 the phosphomimetic TRS120-SαβγD variant tended to be mostly membrane associated, with
337 almost no detectable cytosolic signal (Fig. S13).
338
339

340 **TRS120-SαβγA and TRS120-SαβγD have opposite effects on seed germination under**
341 **osmotic stress**
342 We first analyzed the impact of osmotic stress on the germination frequencies of TRS120
343 phosphovariants. Different TRS120-SαβγA and TRS120-SαβγD primary transformants were
344 plated on media containing 0, 200, or 400 mM mannitol (Fig. 6A-C). As compared with the control
345 (Col-0), the TRS120-SαβγA phosphovariant had higher seed germination rates on mannitol: on
346 day 4 we observed 70% germination in TRS120-SαβγA versus 35% germination for the control
347 on 400 mM mannitol as an osmotic agent (Fig. 6C). In this respect, TRS120-SαβγA was similar to
348 the ABA deficient mutant *aba2-1*, known to be osmotolerant with respect to seed germination (Fig.
349 6C). In contrast, the TRS120-SαβγD phosphovariant exhibited delayed and reduced germination,
350 with lower maximal germination rates, even in the absence of mannitol (Fig. 6A-C). Indeed, on
351 400 mM mannitol TRS120-SαβγD mutants reached a maximal germination rate of 60% compared
352 to 90% for the wild type. With respect to its delay in germination, TRS120-SαβγD was similar to
353 the ABA coreceptor higher order mutant *hab1-1 abi1-2 pp2ca-1*, known to be osmosensitive at
354 germination (Fig. 6C). In summary, the non-phosphorylatable TRS120-SαβγA mutations
355 enhanced whereas the phosphomimetic TRS120-SαβγD mutations reduced germination on
356 mannitol.
357
358 **TRS120 phosphorylation status affects hypocotyl versus root trade-offs under additive**
359 **stress conditions**
360 In light of the decision phenotypes of *bin2* and *trappii* mutants and of the observation that AtSKs
361 such as BIN2 target TRAPPII, the question arises as to whether shaggy-like kinases regulate
362 differential growth decisions via TRS120 phosphorylation. To test this hypothesis, AtTRS120
363 phosphovariants homozygous for the null *trs120-4* allele and hemizygous for the phosphovariant
364 construct were studied under different environmental or stress conditions. The etiolation response
365 was not impacted by the phosphorylation status of AtTRS120 (Fig. S14). In contrast, TRS120
366 phosphomutants had phenotypes under additive stress conditions (Fig. 6D-F; Fig. S15A-C).
367 TRS120-SαβγA non-phosphorylatable variants exhibited an enhanced root response under
368 darkW conditions (Fig. 6E) and a strongly enhanced ratio response to water stress in the dark
369 (mean $RQ_{ratio}$ = 1.49; Fig. 6F). Conversely, the phosphomimetic TRS120-SαβγD mutants exhibited
370 severely attenuated responses to water stress in the dark in all respects (Fig. 6D-F; mean
371 $RQ_{hypocotyl}$= 0.66; mean $RQ_{root}$ = 1.48; mean $RQ_{ratio}$ = 0.44). Thus, the non-phosphorylatable
372 TRS120-SαβγA and the phosphomimetic TRS120-SαβγD mutations had opposite effects on
373 hypocotyl versus root lengths under water stress in the dark, with TRS120-SαβγA exhibiting an

374 enhanced and TRS120-SαβγD an attenuated ratio response (Fig. 6F). Under all environmental
375 conditions, the total seedling length of the phosphovariants did not significantly differ from that of
376 the wild-type AtTRS120 construct (Fig. S15D), which highlights the absence of a growth defect.
377 We conclude that the TRS120 phosphorylation status impacts the seedling's ability to differentially
378 regulate its hypocotyl and root lengths in response to additive stress conditions. Taken together,
379 the data show opposite impacts of non-phosphorylatable versus phosphomimetic mutations at
380 AtTRS120 AtSK sites in terms of seed germination under osmotic stress and responses to additive
381 stress. This suggests that TRAPPII phosphorylation by shaggy-like kinases mediates adaptive
382 responses to osmotic stress and to light and water availability.
383
384 ***bin2* higher order and *trappii* conditional mutants exhibit a synergistic genetic interaction**
385 **with respect to root gravitropism**
386 To further address the physiological significance of the BIN2-TRAPPII interaction *in vivo*, we
387 deployed higher order mutant analysis. This approach, however, was challenged by (i) the
388 functional redundancy between BIN2 and its homologues (Vert & Chory, 2006; Yan *et al*, 2009),
389 (ii) the semi-dominant nature of *bin2-1*, (iii) the seedling lethality of *trappii* null alleles, as well as
390 (iv) the pleiotropic phenotypes of both *bin2-1* and *trappii* dwarfs (Li *et al*, 2001; Thellmann *et al*,
391 2010; Ravikumar *et al*, 2018; Garcia *et al*, 2020). To address these challenges, we engineered a
392 conditional *trs120* knock-down allele, named *trs120i*. This features an artificial microRNA that
393 targets 5' AtTRS120/TRAPPC9 sequences, expressed under an estradiol-inducible promoter (Fig.
394 7A; Curtis & Grossniklaus, 2003). The *trs120i* construct was introduced into the wild type (Col-0)
395 and into the *bin2-3bil1bil2* triple knock-out mutant. Upon induction, *trs120i* exhibited a mild and
396 *bin2-3bil1bil2* a more pronounced root agravitropism (Fig. 7B-C). The *bin2-3bil1bil2 trs120i* higher
397 order mutant had a more than additively enhanced agravitropic response upon induction as
398 compared to *trs120i* or *bin2-3bil1bil2* alone (Fig. 7B-C, 7E). This was evidenced as primary roots
399 growing in all directions, often against gravity at 180° in *bin2-3bil1bil2 trs120i* (Fig. 7B-C). We
400 observed synthetic enhancement specifically upon estradiol induction and not in the mock control
401 (Fig. 7D, compared to 7E). This is indicative of a synergistic genetic interaction. Furthermore, it
402 suggests that adaptive growth decisions such as gravitropism are mediated by the BIN2/AtSK-
403 TRAPPII interaction.
404
405

406 **DISCUSSION**

407 In this study, we explore the role of the TGN in stress responses in Arabidopsis. Our point of entry
408 is the TRAPPII complex, which has been shown to be required for TGN structure and function (Qi
409 *et al*, 2011; Ravikumar *et al*, 2018). We performed proteomic and yeast two-hybrid screens and
410 present several lines of *in vitro* (Y2H, kinase assays) and *in vivo* (IP-MS, pharmacological
411 inhibition) evidence that the TRAPPII subunit AtTRS120/TRAPPC9 is the target of AtSK kinases,
412 including BIN2. We document differential phosphorylation of three distinct AtSK/GSK3 sites by
413 three of the four AtSK clades. The phosphorylation status of AtTRS120 impacted seed germination
414 under osmotic stress as well as adaptive responses to additive stress *in planta*. We show that *bin2*
415 and *trappii* alleles have related phenotypes with respect to an impaired adaptation to additive
416 stress conditions, in this instance achieved by the simultaneous withdrawal of light and water.
417 Furthermore, *bin2* higher order and *trappii* conditional mutants exhibited a synergistic genetic
418 interaction with respect to root gravitropism.

419 Like other tropisms, root gravitropism requires organ bending as a result, at least in part, of the
420 differential sorting of PIN transporters (Friml *et al*, 2002; Ding *et al*, 2011; Konstantinova *et al*,
421 2021). PIN2 polarity has been shown to be abolished in *trappii* mutants (Qi *et al*, 2011; Rybak *et*
422 *al*, 2014) and to require TGN function (Naramoto *et al*, 2014; Qi *et al*, 2011; Rybak *et al*, 2014;
423 Ravikumar *et al*, 2018). A concern when assessing the role of the TGN in adaptive or stress
424 responses is that TGN-related mutants typically have pleiotropic phenotypes as a consequence
425 of their impairment in fundamental processes such as secretion, endocytosis or sorting (Rosquete
426 & Drakakaki, 2018; Ravikumar *et al*, 2018). To distinguish between primary defects in growth on
427 the one hand and adaptive responses on the other, we monitored trade-offs between hypocotyl
428 and root growth under additive stress conditions (Kalbfuß *et al*, 2022). We focus on *echidna* and
429 *trappii* mutants as these have been shown to impact both the structure and the function of the
430 TGN (Boutté *et al*, 2013; Gendre *et al*, 2011, 2013; McFarlane *et al*, 2013; Qi *et al*, 2011;
431 Ravikumar *et al*, 2018). These TGN mutants had hypocotyl and root growth defects, which are
432 characteristic of trafficking mutants (Fig. S10). In addition to their growth defects, *trappii trs120-4*
433 mutants had a significant hypocotyl response but in the wrong orientation as compared to the wild
434 type (denoted by red asterisks in Fig. 4, Fig. 5 and Fig. S11) as well as an insignificant
435 hypocotyl/root ratio response to light and water deprivation (Fig. 4). The *trappii* phenotypes
436 described in this study are difficult to explain as mere growth defects. Rather, the inability to
437 mediate growth trade-offs in response to additive stress provides a compelling argument for
438 TRAPPII as having a role in adaptive growth decisions.

439 Conceptually, the optimization of hypocotyl-to-root ratios can be deconstructed into four distinct
440 stages: (i) perception, (ii) signal integration, (iii) decision making and (iv) the implementation of
441 resulting actions (Kalbfuß *et al*, 2022). To address the first stage, perception, we looked at, for
442 example, quadruple *phyAphyBcry1cry2* photoreceptor mutants; these failed to adjust their organ
443 lengths to light versus dark conditions but had a highly significant response to additive stress (Fig.
444 4G-H; Fig. S8A; Fig. S9; Fig. S10G-I; Kalbfuß *et al*, 2022). The opposite was true for *bin2-3bil1bil2*
445 and *trappii* mutants, which were able to respond to single stress factors but not to additive stress
446 (Fig. 4; Fig. 5; Fig. S11; Kalbfuß *et al*, 2022). Shaggy-like kinases integrate a vast number of
447 signaling pathways (Lv & Li, 2020; Youn & Kim, 2015; Li *et al*, 2021; Song *et al*, 2023; Planas-
448 Riverola *et al*, 2019). Accordingly, we have postulated that the *bin2-3bil1bil2* "decision" phenotype
449 under conflict-of-interest scenarios is primarily due to signal integration (Kalbfuß *et al*, 2022).
450 Prime candidates for the fourth stage, execution or implementation of the action, are *echidna*
451 mutants, which are impaired in the formation of secretory vesicles and cell elongation (Boutté *et*
452 *al*, 2013; Gendre *et al*, 2013; McFarlane *et al*, 2013); these had highly significant adaptive
453 responses - in the correct orientation - despite their growth defects (Fig. 4E). The question arises
454 as to how to categorize *trappii* mutants in the above conceptual framework. Despite having
455 abnormally short hypocotyls or roots, *trappii* mutants still exhibited differential length increase
456 depending on light availability (Fig. S10). This shows that they are able to perceive and respond
457 to light.
458 If TRAPPII is primarily involved neither in perception nor in execution, this would place it at the
459 signal integration and/or decision-making steps of adaptive growth decisions. The TRAPPII
460 interactome is vast and complex, with - in addition to the expected ontologies describing traffic,
461 transport and cellular organization - a surprising number of signaling components implicated in
462 responses to abiotic cues (Fig. 1; Fig. S1). This suggests a role for TRAPPII in signal integration.
463 A recent study of the BIN2 signaling network describes the expected components of hormone
464 signaling, phototropism and stress responses; surprisingly, the BIN2 signaling network also
465 includes secretion, endocytosis, autophagy, TGN, endoplasmic reticulum (ER), cell wall and
466 cytoskeleton (Kim *et al*, 2023). Thus, there is a considerable compartmental overlap between the
467 BIN2 network and the TRAPPII interactome. Nonetheless, TRAPPII was not reported among the
468 482 members of the BIN2 signaling network identified by proximity labeling (Kim *et al*, 2023). The
469 discrepancy could be due to the different methods used: yeast two hybrid and proteomics in this
470 study versus proximity labelling and phosphoproteomics in Kim *et al* (2023). However, a
471 multiomics approach identified AtTRS120-S971 (encompassed by our identified β site AtTRS120-
472 S971:S973:S974:S975) as being differentially phosphorylated in response to brassinolide

473 treatment (Clark *et al*, 2021). This provides an additional line of *in vivo* evidence for a BIN2-
474 AtTRS120 interaction and, consistently with our PPZ experiment (Fig. S6), suggests that TRAPPII
475 phosphorylation is, at least in part, brassinosteroid-regulated.
476 BIN2 is a negative regulator of BR signaling and AtSK11 and AtSK12 have been shown to
477 negatively regulate root growth responses under osmotic stress (Dong *et al*, 2020; Li *et al*, 2021;
478 Song *et al*, 2023). To explore the biological significance of the AtSK-TRAPPII interaction, we
479 probed the phenotypes of TRAPPII phosphovariants. We found that these had an impact on
480 hypocotyl versus root growth trade-offs in response to additive stress (Fig. 6D-F). Furthermore,
481 the non-phosphorylatable TRS120-SαβγA variant had an enhanced root adaptation whereas the
482 phosphomimetic variant decreased root growth under additive stress (Fig. 6D-F), which is
483 consistent with the negative regulation of growth by BIN2 and other AtSKs. We have previously
484 described plant-specific domains or subunits predicted to be at the dimer interface of the
485 Arabidopsis TRAPPII complex (marked in green in Fig. 2D; Garcia *et al*, 2020; Kalde *et al*, 2019).
486 Interestingly, BIN2 interacts with the plant-specific C-terminal domain of AtTRS120, while MAP65-
487 3 interacts with plant-specific C-terminal domains of the TRAPPII-specific subunits
488 CLUB/AtTRS130 and AtTRS120 (Steiner *et al*, 2016). This presents intriguing implications
489 regarding the potential role of the AtSK-TRAPPII module in meeting the unique demands of
490 endomembrane traffic in plants. Plant and animal cells differ in numerous ways, many of which
491 can be attributed to the presence of the plant cell wall. Novel or expanded families of vesicle-
492 trafficking genes are implicated in cell wall assembly (Assaad, 2001). Cell wall deposition and
493 remodeling underly any growth response in plants. Growth in the face of challenging, restrictive
494 environments is a distinctive survival strategy unique to plants (Assaad, 2001). In this study, we
495 look at the tight regulation of differential growth that enables plants to thrive under multiple stress
496 conditions, in the absence of a carbon or energy source.
497 The observation that the *trappii* "decision" phenotype was not shared by *echidna* mutants raises
498 the question as to what facet of TGN function is required for responses to additive stress.
499 ECHIDNA and TRAPPII have been shown to have overlapping roles in basal TGN functions such
500 as secretion (Ravikumar *et al*, 2018). In addition, ECHIDNA regulates ER stress and immunity
501 whereas TRAPPII has roles in cytokinesis and in the establishment of cell polarity that appear to
502 be independent of ECHIDNA (Liu *et al*, 2023; Ravikumar *et al*, 2018). In the literature, there are
503 few examples of null mutants that are associated with the TGN and that have a positive influence
504 on growth. One such example is ZmBet5L1 (Zhao *et al*, 2023), which encodes a core subunit of
505 the TRAPPII complex (Kalde *et al*, 2019; Thellmann *et al*, 2010). Null alleles of ZmBet5L1 enhance
506 root growth also in the absence of stress (Zhao *et al*, 2023). The TRAPPII complex has two distinct

507 possible molecular functions. First, it has been postulated to act as a multisubunit tethering
508 complex, even though direct evidence is lacking (Ravikumar *et al*, 2017; Brunet & Sacher, 2014;
509 Kim *et al*, 2016; Pinar *et al*, 2019). Second, it has been shown to act as a Rab GTPase Guanine
510 nucleotide Exchange Factor (Rab-GEF; Cai *et al*, 2005; Morozova *et al*, 2006; Pinar *et al*, 2015;
511 Thomas & Fromme, 2016; Riedel *et al*, 2018). Rab-GEFs act as central cellular switches that can
512 activate Rab GTPase cascades, which are in turn crucial for the development of polarity and
513 directional growth in plants (Elliott *et al*, 2020). Indirect *in vivo* evidence suggests that Arabidopsis
514 TRAPPII acts as a GEF for Rab-A GTPases, orthologues of the RAB11/Ypt31 families known to
515 be activated by fungal and metazoan TRAPPII (Qi & Zheng, 2011; Kalde *et al*, 2019). In
516 Arabidopsis, Rab-A GTPases are TGN-associated and comprise a highly expanded class with 26
517 members (Kalde *et al*, 2019; Elliott *et al*, 2020). In contrast to ECHIDNA, which is required for the
518 biogenesis of secretory vesicles and for growth generically, as a putative Rab-A GEF TRAPPII
519 has an ability to mediate all the highly diverse facets of TGN function. In a judgement-decision
520 model for plant behavior, judgment is a composite of discrimination, assessment, recognition, and
521 categorization (Karban & Orrock, 2018). In this context, it is noteworthy that the most expanded
522 Rab GTPase family is TGN-associated, suggestive of a tremendous degree of discrimination,
523 specialization and subcompartmentalization at the TGN. Atomic structures of yeast and metazoan
524 TRAPPII depict a conserved triangular structure around the central active site chamber in which
525 TRS120/TRAPPC9 and TRS130/TRAPPC10 form tongs that hold the core complex in place
526 (Galindo *et al*, 2021; Mi *et al*, 2022; Bagde & Fromme, 2022). In a cross-kingdom structural
527 alignment, AtTRS120 and CLUB/AtTRS130 aligned along their yeast orthologues in the same
528 overall structure (Fig. S4). In yeast, TRS120/TRAPPC9 has been proposed to comprise a lid that
529 encloses the active site chamber of the TRAPPII GEF (Bagde & Fromme, 2022). Interestingly, the
530 β and γ phosphorylation sites we have identified in AtTRS120/TRAPPC9 face the active site
531 chamber, including the RAB11/Rab-A binding pocket, proposed by Mi *et al* (2022) and Bagde &
532 Fromme (2022) (Fig. S4A). It is, therefore, tempting to speculate that the phosphorylation status
533 of AtTRS120/TRAPPC9 modulates the specificity of the putative GEF activity of Arabidopsis
534 TRAPPII (Kalde *et al*, 2019).
535 Our study highlights the possible relevance of the AtSKs-TRAPPII interaction for adaptive growth
536 decisions (Fig. 8). Shaggy-like kinases such as BIN2 integrate a vast number of signaling
537 pathways and, together with receptor complexes at the cell surface, comprise a surveillance
538 system fine-tuned to both biotic and abiotic cues (Lv & Li, 2020; Planas-Riverola *et al*, 2019; Youn
539 & Kim, 2015; Li *et al*, 2021; Song *et al*, 2023). Via the cytosol, the AtSKs would then transmit this
540 information by mediating the phosphorylation status of the TRAPPII complex. TRAPPII would, in

541 turn, mediate TGN function. As an early endosome, the TGN is a central hub in the flow of
542 information to and from the cell surface. It is also intimately connected to the late endosome (or
543 the pre-vacuolar compartment) and to the Golgi, which provides complex polysaccharides as
544 building blocks for the deposition of new cell walls. Thus, the AtSK-TRAPPII interaction would
545 integrate all levels of cellular organization. We posit that signal integration and decision-making
546 occur at the AtSK-TRAPPII interface and that, downstream of TRAPPII, Rab GTPase cascades
547 are implicated in implementing decisions reached at the AtSK-TRAPPII module (Fig. 8). Sorting
548 and trafficking decisions at the TGN would enable plants to respond to developmental or
549 environmental signals via differential growth or various forms of movement.
550 Plants exhibit plasticity in their growth, meaning they can adjust their growth patterns in response
551 to environmental cues such as light, temperature, and nutrient availability. It has been argued that
552 plant phenotypic plasticity "is the result of signal integration - a process that requires cell-cell
553 communication, and that results in adaptive forms of movement not to be interpreted as automatic
554 and programmed" (Garzón & Keijzer, 2011). Movement in plants involving organ bending require
555 the polar distribution of morphogens such as auxin. This, in turn, requires the polarized localization
556 of auxin transporters such as PINs. The Arabidopsis TRAPPII complex has been shown to play a
557 pivotal role in a variety of sorting decisions including the polar localization of PIN2 proteins (Qi *et*
558 *al*, 2011; Rybak *et al*, 2014; Ravikumar *et al*, 2018). How environmental or developmental cues
559 regulate the cargo composition and sorting of TGN vesicles remains unclear. Future experiments
560 will explore the impact of the TRAPPII phosphorylation status on protein sorting, cell polarity, and
561 on the Rab specificity of TRAPPII as a putative GEF. Furthermore, downstream components that
562 govern physiological changes in response to TRAPPII phosphorylation will need to be determined.
563 The presence of the TOR kinase in the TRAPPII interactome is intriguing, as TOR integrates
564 information about nutrient and energy availability, and has recently been shown to regulate actin
565 dynamics as a function of ATP levels (Dai *et al*, 2022); it is tempting to speculate that TOR could
566 provide information on nutrient and energy levels to the AtSK-TRAPPII "decision" module. In
567 plants, the Trans-Golgi Network (TGN) plays a critical role in the relay of information between the
568 cell surface and intracellular compartments. An AtSK-TRAPPII interaction would instruct the TGN,
569 a central and highly discriminate cellular hub, as to how to mobilize and allocate resources to
570 optimize survival under limiting or adverse conditions.
571

572 **EXPERIMENTAL PROCEDURES**
573
574 **Lines and growth conditions**
575 All the lines used in this study are listed in Table S1 (mutant alleles) or in the Supplementary
576 Methods (phosphovariants). Seedling-lethal mutants were propagated as hetero- or hemizygotes.
577 Insertion lines were selected via the TAIR and NASC web sites (Swarbreck *et al*, 2008). Plants
578 were grown in the greenhouse under controlled temperature conditions and with supplemental
579 light, or under controlled growth chamber conditions at the TUMmesa ecotron (16/8 h photoperiod
580 at 180 µmol $m^{-2}s^{-1}$). Seeds were surface sterilized, stratified at 4°C for two days and plated on ½
581 MS medium supplemented with 1% sucrose and B5 Vitamins (Sigma;
582 https://www.sigmaaldrich.com). Plates were incubated at 22°C in constant light (80 µmol $m^{-2}s^{-1}$).
583 The root tips of five-day-old plate-grown seedlings were used for confocal microscopy. Seven-
584 day-old plate-grown seedlings were used for co-immunoprecipitation.
585
586 **Co-immunoprecipitation (IP)**
587 For CLUB/AtTRS130:GFP we used 3 g of inflorescences per IP experiment. For TRS120:GFP, 3
588 g of light-grown seedlings were harvested at day 7. For bikinin treatment, seedlings were treated
589 for 30 min with 25 µM bikinin at day 7. For PPZ treatment, 5-day-old seedlings were treated with
590 2 µM PPZ for 48 h; respective mock treatments were conducted in parallel.
591 Co-immunoprecipitation experiments were carried out as described previously (Rybak *et al*, 2014).
592 Briefly, seedling lysates were incubated with GFP-trap beads (Chromotek). After washing away
593 all non-binding proteins, 70 µl 2x NuPAGE LDS + 25 mM dithiothreitol (DTT) buffer (ThermoFisher,
594 US) was added and boiled at 70°C for 10 min to denature the bait and all interaction partners.
595 In-gel trypsin digestion was performed according to standard procedures (Shevchenko *et al*,
596 2006). Briefly, the samples were run on a NuPAGE 4-12% Bis-Tris Protein Gel (Thermofisher
597 Scientific, US) for 3 min. Subsequently, the still not size-separated single protein band per sample
598 was cut out of the gel, reduced (50 mM DTT), alkylated (55 mM chloroacetamide) and digested
599 overnight with trypsin (trypsin-gold, Promega). The resulting peptides were analysed by mass
600 spectrometry. More detailed information on the mass-spectrometric data acquisition is provided in
601 the supporting method section. See data deposition for access to the raw data.
602
603 **Molecular techniques and site directed mutagenesis (SDM)**
604 For subcloning for expression in *Escherichia coli* (*E. coli*) or yeast, we used cDNA clones
605 developed by the plant genome project of RIKEN Genomic Sciences Center (Seki *et al*, 1998,
606 2002). Non-phosphorylatable and phosphomimetic TRS120 phosphosite variant constructs (SαA,
607 SβA, SγA, SαβA, SαγA, SβγA, SαβγA and SαD, SβD, SγD, SαβD, SαβγD)) were generated using
608 the GATEWAY® cloning system and site-specific primers (see supplementary methods for
609 substituted amino acids and used primers). TRS120-T2 cDNA sequences (spanning amino acids
610 499-1187; Rybak *et al*, 2014) were used as SDM template for protein expression in *E. coli* (kinase
611 assays) and in yeast (Y2H). For *in planta* experiments (confocal microscopy, stress assays), the
612 genomic construct $P_{TRS120}$::TRS120:GFP (Rybak *et al*, 2014) was used as an SDM template.
613 TRS120 phosphovariants were introduced into plants via *Agrobacterium* mediated transformation
614 (see supplementary methods for further details).
615

616
617 **Generation of inducible *trs120* knock-down lines**
618 To generate an inducible *trs120* knock-down mutant, named *trs120i*, an artificial microRNA
619 targeting the 5' end of AtTRS120 was designed with the Web MicroRNA Designer 3 (Schwab *et*
620 *al*, 2006). The designed amiRNA sequence (5'-TATAACTCTTACAAGCGGCAT-3') was
621 introduced in the miR319a precursor and synthesized as a gene strand (Eurofins) with attached
622 attB sites for the GATEWAY® cloning system. The TRS120 amiRNA precursor was cloned into
623 the estradiol inducible pMDC7 vector (Curtis & Grossniklaus, 2003) and introduced into plants via
624 *Agrobacterium* mediated transformation (see supplementary methods for further details and full
625 gene strand sequence).
626
627 **Yeast two-hybrid (Y2H)**
628 Y2H pairwise tests were performed as described in Altmann *et al* (2018). Briefly, open reading
629 frames (ORFs) encoding CLUB/AtTRS130 truncations (C2, C3), TRS120 truncations (T1, T3) and
630 BIN2 were transferred by Gateway cloning into the GAL4 DNA-binding domain (DB) encoding
631 Y2H vector pDEST-pPC97, and subsequently transformed into the yeast strain Y8930. These
632 constructs were screened by yeast mating against TRAPPII subunits and truncations thereof
633 (CLUB-C1, -C2, -C3 and TRS120-T1, -T2, -T3) or the TRS120-T2 truncation and its
634 phosphomutants TRS120-T2 SαD, SβD, SγD, SαβD and SαβγD fused to the GAL4 activation
635 domain (AD) in the yeast strain Y8800. Interaction was assayed by growth on selective plates
636 using the *HIS3* reporter, and using 1 mM 3-Amino-1,2,4-triazole (3-AT) to suppress background
637 growth. All candidate interactions were verified by pairwise one-on-one mating in four independent
638 experiments. Only pairs scoring positives in all four assays were considered as *bona fide*
639 interaction partners. The use of low-copy plasmids, weak promoters, the counter-selectable
640 marker $cyh2^S$ on the AD-Y plasmid as well as semi-quantitative scoring of quadruplicate tests has
641 been shown to reliably eliminate experimental artifacts and hence false-positives. With the
642 exception of the CLUB-C1 truncation, all TRAPPII truncations and catalytic core subunits used as
643 DB clones in pair-wise tests yielded at least one positive interaction (see also Kalde *et al*, 2019;
644 Garcia *et al*, 2020) and this was used as an internal positive control for the interpretation of
645 negative interaction data.
646
647 ***In vitro* kinase assays**
648 Glutathione S-transferase (GST):BIN2 (Li & Nam, 2002) and GST:TRS120-T2 WT or
649 phosphovariants were expressed in *Escherichia coli* (Rosetta-gami™ strain) under constant
650 shaking for 20 h at 25°C or 20 h at 18°C, respectively. The expressed proteins were affinity purified
651 with GST-tags. After sonication of the samples in 1x PBS, 1 mM PMSF, 1 mg/ml lysozyme and
652 1% Triton X-100, the bacterial cell rests were centrifuged for 30 min at 16,000 g. Supernatants
653 were incubated for 2 h with Glutathione Sepharose® 4 Fast Flow Beads (GE Healthcare) while
654 rotating. After washing the samples five times, the GST tagged proteins were eluted with 10 mM
655 glutathione and concentrated by ultra-filtration.
656 *In vitro* kinase assays with radiograph readout were performed as described previously (Kim *et al*,
657 2012), with some adaptations. In short, ca. 0.1 µg GST:BIN2 and ca. 0.5 µg of GST:TRS120-T2
658 WT or phosphovariant were incubated in 20 mM Tris pH 7.5, 1 mM $MgCl_2$, 100 mM NaCl, 1 mM
659 DTT, 100 µM ATP and 10 µCi ATP[$\gamma$-$^{32}$P] for 3 h at 22°C in motion. The kinase reaction was

660 stopped by adding 2x SDS sample buffer and by boiling the samples for 10 min. Protein
661 phosphorylation was analyzed by autoradiographs and SDS-PAGE.
662 *In vitro* kinase assays with mass-spectrometry readout were performed to determine specific
663 phosphorylation sites. For each reaction, 10 µg of substrate (TRS120-T2) and different dilutions
664 of the kinase (undiluted, 1:5, 1:10, 1:20 or 1:100 as indicated in the figure panels) were incubated
665 for 15, 30, and 120 min in a kinase buffer (20 mM Tris HCl pH 7.8, 100 mM NaCl, 1 mM $MgCl_2$, 1
666 mM DTT, 1 mM ATP). For the negative controls, one sample with the highest kinase concentration
667 and the longest incubation time was incubated in a kinase buffer without ATP. For the kinase dead
668 control, the kinase was heat-inactivated prior to the incubation with its substrate. To stop the
669 reaction, samples were heated at 95°C for 5 min. After reduction (10 mM DTT), alkylation (55 mM
670 CAA) and protein digestion (trypsin-gold, Promega) the resulting peptides were purified using self-
671 packed StageTips (C18 material, 3M Empore) and analyzed by mass spectrometry. More detailed
672 information can be found in the supporting methods.
673
674 **LC-MS/MS data acquisition and analysis**
675 Generated peptides were analyzed on a Dionex Ultimate 3000 RSLCnano system coupled to a
676 Q-Exactive HF-X mass spectrometer (Thermo Fisher Scientific) in data-dependent acquisition
677 mode. Peptide identification and quantification was performed using the software MaxQuant
678 (version 1.6.1.0) (Cox & Mann, 2008; Tyanova *et al*, 2016a) with its built-in search engine
679 Andromeda (Cox *et al*, 2011) and an *Arabidopsis thaliana* reference database (Araport). Perseus
680 (Tyanova *et al*, 2016b) and Python 3.0 were used for statistical data analyses. For a targeted
681 analysis of the kinase assay data set, MS1 chromatograms from selected phosphopeptides were
682 extracted and analyzed using the Skyline software (MacLean *et al*, 2010). For detailed information
683 about LC-MS/MS data acquisition and analysis see supporting methods.
684
685 **Light and electron microscopy**
686 For scanning electron microscopy, a Zeiss (LEO) VP 438 microscope was operated at 15 kV.
687 Fresh seedlings were placed onto stubs and examined immediately in low vacuum. Confocal
688 microscopes used for imaging were an Olympus (www.olympus-ims.com) Fluoview 1000 confocal
689 laser scanning microscope (CSLM) and a Leica (www.leica-microsystems.com) SP8 Hyvolution
690 CSLM. 40x and 60x water immersion 0.9 numerical aperture objectives (Olympus) were used.
691 Imaging data were acquired using LAS-X software (Leica) and FV10-Ver.2.6.0 software
692 (Olympus). GFP fluorescent proteins were imaged with 488 nm excitation and 500-550 nm
693 emission. 10-day-old seedlings were stained with modified pseudo-Schiff propidium iodide
694 staining (Truernit *et al*, 2008). Excitation Laser was set to 488 nm. The Emission was detected at
695 520 nm. The junction between the meristematic and elongation zones was determined by marking
696 the first cell in a single cortex cell file that was double the length of the previous cell (González-
697 García *et al*, 2011). For seedling images, a Leica S APO stereo microscope with a Leica MC170
698 HD camera was used.
699
700 **Differential growth decision assay**
701 The differential growth decision experiment was performed as described by Kalbfuß *et al* (2022).
702 In brief, seeds were surface sterilized using a brief 80% ethanol rinse followed by 15 min
703 incubation in sterilization buffer (0.01% SDS, 3% NaOCl). After 5 washes in mQ water, seeds

704 were resuspended in 0.15% agar and stratified in the dark at 4°C for 7 days to break seed
705 dormancy. Afterwards, seeds were plated on squared plates with exactly 45 ml ½ MS medium
706 supplemented with B5 Vitamins (Sigma). Culture media for TRS120 phosphomutants was
707 additionally supplemented with 50 µg/ml kanamycin to select for transgenic seedlings. For -0.4
708 MPa water deficit, media plates were infused with sterile-filtrated 45 ml 2x PEG-6000 (Merck
709 group; dissolved in liquid ½ MS media) for exactly 24 h at RT and afterwards the PEG-solution
710 completely decanted. Seeds were plated at the interface between the culture media and sterilized
711 plastic strips on the media such that, upon germination, only the root touched the agar. For water
712 stress, seeds in each biological replicate were sown on two plates for technical replicates which
713 were pooled for analysis. After plating, plates were sealed with breathable tape. Plates for dark
714 conditions were wrapped with two layers of thick aluminum foil. All plates were incubated for 10
715 days at 22°C with permanent light (80 µmol $m^{-2}s^{-1}$). Note that the plates were negatively inclined
716 by 4° to promote root growth on the media surface rather than in the agar.
717 After incubation of 10 days seedlings were transferred onto cold 1.2% agar plates, scanned at
718 1200 ppi and saved as tiff files. Hypocotyl and root lengths were analyzed with Fiji - ImageJ using
719 the free-hand-tool. The ratio was calculated as hypocotyl length divided by root length.
720 Root and hypocotyl responses to water deficit in the dark (abbreviated as darkW) were computed
721 as

722 $$\frac{\text{organ length in the dark}}{\text{organ length under darkW}}$$

723

724 Because the hypocotyl and root have opposite responses to our additive stress conditions
725 (hypocotyl length decreases but root length increases in response to water stress in the dark, as
726 shown in Fig. 4) the RQs move in opposite directions.
727 The ratio was computed as follows:

728 $$\text{ratio adjustment}=\frac{\left(\frac{\text{hypocotyl}}{\text{root}}\right)\text{dark}}{\left(\frac{\text{hypocotyl}}{\text{root}}\right)\text{darkW}}$$

729 Due to variability between PEG lots and PEG plates (Kalbfuß *et al*, 2022), we normalized each
730 mutant to the corresponding wild-type ecotype (see Table S1) on the same plate. Thus, the
731 normalized ratio adjustment to water stress in the dark (darkW) was computed as follows:

732 $$RQ_{ratio}=\frac{\text{ratio adjustment mutant}}{\text{ratio adjustment wild type}}$$

733

734 $RQ_{hypocotyl}$ and $RQ_{root}$ as well as light versus dark responses were computed in a similar fashion
735 (Fig. S9, S10, S14). These normalized organ and ratio adjustments were referred to as response
736 quotients (RQ) to light-to-dark or dark-to-darkW conditions. The mean $RQ_{ratio}$ of at least three
737 biological replicates (i.e. the seed stocks from different mother plants) is shown. Please see
738 Supporting Table S3 for thresholds for attenuated, normal, versus enhanced organ or ratio
739 responses. For volcano plots we plotted the mean $RQ_{ratio}$ on the X axis and the median $P_{ratio}$-value
740 on the Y axis. Organ and ratio adjustments for light-to-dark comparisons were computed as organ
741 length (or ratio) in the light divided by organ length (or ratio) in the dark. *P*-values were computed
742 with the student's t-test. Responses were considered to be insignificant for *P*-values ≥ 0.05 and

743 attenuated for *P*-values ≥ 0.00001. The median *P*-value for at least three replicates is shown in
744 the volcano plots.
745
746 **Germination assay under osmotic stress**
747 For germination curve experiments, surface-sterilized seeds were stratified in the dark at 4°C for
748 two days. Seeds were plated on ½ MS media supplemented with 0.05% B5 Vitamins (Sigma) and
749 either 0 mM, 200 mM, or 400 mM mannitol (Millipore). Approximately 100 seeds were plated per
750 condition. Plates were incubated at 22°C under constant light conditions (80 µmol $m^{-2}s^{-1}$) and
751 rotated every day to avoid light effects. Seed germination rates were recorded every 24 h. Seeds
752 were scored as germinated when the radicle emerged. Data were obtained for three biological
753 replicates, each with three technical replicates.
754
755 **Root gravitropism assay**
756 *trs120i* lines were selected on ½ MS media supplemented with 20 µg/ml hygromycin B. Control
757 lines were grown in parallel on media without antibiotics. After 4 days, seedlings were transferred
758 to ½ MS media supplemented with 20 µM β-estradiol (Est; 20 mM stock dissolved in EtOH; Sigma)
759 or 0.1% EtOH as mock control and grown vertically for additional nine days. The primary root tip
760 angles (excluding lateral roots) were analyzed with Fiji - ImageJ. Primary roots exhibiting looping
761 (see yellow arrow in Fig. 7B) were scored as -180° due to their growth against gravity. Primary
762 root growth orientation was visualized as frequency plots in a polar coordinate system in R. To
763 quantify agravitropic roots, the frequency of primary root tips growing against gravity (angles < -
764 90° and > 90°) was counted per experiment.
765
766 **Western blot analysis**
767 Standard Western blot analysis was performed according to Sambrook *et al* (1989). 7.5% SDS-
768 PAGE gels (Mini-PROTEAN TGX gels, Bio-Rad) were blotted onto PVDF Immobilon-FL
769 membranes (Millipore). Polyclonal rabbit anti-GFP antibody (1:2000; A11122, Invitrogen) was
770 used as primary antibody. As secondary antibody, we used a goat anti-rabbit Horseradish
771 peroxidase-conjugated antibody (1:6000; Pierce, Thermo Scientific) together with the SuperSignal
772 West Femto Maximum Sensitivity Substrate (Thermo Scientific). To check for equal loading, blots
773 were stained with Coomassie (10% acetic acid, 50% methanol, 0.25% Coomassie Blue R-250)
774 and subsequently destained (10% acetic acid, 50% methanol).
775
776 **Data analysis and image processing**
777 False discovery rates, determined with the standard two-tailed t-test, were set at a cut-off of 1.
778 Images taken with the Leica SP8 microscope were deconvolved using the built-in Huygens
779 Scientific deconvolution software (www.leica-microsystems.com) operated in 2D. For consistency,
780 we selected cortical root tip cells, at a height of 6-22 cells above the quiescent center in the root
781 apical meristem. Images were processed with Adobe photoshop (www.adobe.com) and GIMP
782 (https://www.gimp.org) and analysed with Image J (https://imagej.nih.gov). Statistical analyses
783 were performed in RStudio. Figures were created with RStudio's ggplot2 package and assembled
784 with Inkscape (https://inkscape.org). Please see the supporting methods for the analysis of mass
785 spectrometry datasets and for multiple sequence and structural alignments.
786

**Acknowledgements**

We thank Prof. Wilfried Schwab, Prof. Erwin Grill and other members of the botany department for their support. Thanks to Prof. Arne Skerra, Martin Schlapschy and Veder Garcia for useful suggestions. We thank Yannik Schreckenberg, Andreas Czempiel, Theo Kalmbach, Hermine Kienberger, Nina Lomp and Franziska Hackbarth for technical assistance. We thank the WZW/TUM Centre for Advanced Light Microscopy (CALM), headed by Ramon Torres-Ruiz and Klaus Michel, for access to confocal microscopes, and Prof. Kay Schneitz for access to their Leica S APO stereo microscope. Thanks to Roman Meier at the TUMmesa facility, directed by Leonardo Teixeira and Bálint Jákli, for supporting us with optimal growth conditions for our plants. Jorge José Casal, Sean Cutler and Ueli Grossniklaus shared published resources.

**Data deposition**

The CLUB:GFP IP-MS data has previously been published (Kalde *et al*, 2019) and deposited to the ProteomeXchange Consortium via the Proteomics IDEntification (PRIDE) partner repository (Perez-Riverol *et al*, 2019). The dataset can be accessed with the identifier PXD013016. All other IP-MS or MS datasets are being deposited here for the first time. New proteomics raw data (*in vitro* kinase assays and *in vivo* evidences with AtTRS120:GFP IP-MS of bikinin and PPZ treated seedlings) including MaxQuant search results and used protein sequence databases can be accessed via Panorama Public (Sharma *et al*, 2014, 2018) with the following link https://panoramaweb.org/phosphoTRAPP_Ara.url.

**Funding**

This work was supported by Deutsche Forschungsgemeinschaft DFG grants AS110/5-2, AS110/8-1 & AS110/10-1 as well as BaCaTEC Nr. 14 [2018-2] to F.F.A., by the European Research Council's Horizon 2020 Research and Innovation Programme (Grant Agreement 648420) grant to P.F-B., and by National Institutes of Health (R01GM066258 to Z.-Y.W.). M. Abele and C.L. were supported by the EU Horizon 2020 grant Epic-XS. TUMmesa was funded with support of the German Science Foundation (DFG, INST 95/1184-1 FUGG).

**Conflict of interest**

The authors declare no conflict of interest.

**Author contributions**

Conceptualization: FFA
Methodology: MA, CL, BA, CHP, PFB, CW, AS, NK, ASM, BB, CM, EF, FFA
Investigation: CW, MA, BA, MAM, AS, NK, ASM, RR, CHP, BB, CM, EF, FFA
Visualization: CW, MA, BA, MAM, AS, NK, ASM, RR, CHP, BB, CM
Funding acquisition: DWE, PFB, ZW, CL, FFA
Project administration: FFA
Supervision: EF, DWE, PFB, ZW, CL, FFA
Writing - original draft: FFA, CW
Writing - review & editing: CW, MA, BA, NK, ASM, RR, CHP, BB, CM, PFB, ZW, CL, FFA

## REFERENCES


Altmann M, Altmann S, Falter C & Falter-Braun P (2018) High-Quality Yeast-2-Hybrid Interaction Network Mapping. *Curr Protoc Plant Biol* 3: e20067

Asaoka R, Uemura T, Ito J, Fujimoto M, Ito E, Ueda T & Nakano A (2013) Arabidopsis RABA1 GTPases are involved in transport between the trans-Golgi network and the plasma membrane, and are required for salinity stress tolerance. *Plant J* 73: 240–249

Assaad FF (2001) Of weeds and men: what genomes teach us about plant cell biology. *Curr Opin Plant Biol* 4: 478–487

Assaad FF, Huet Y, Mayer U & Jürgens G (2001) The Cytokinesis Gene KEULE Encodes a Sec1 Protein That Binds the Syntaxin KNOLLE. *J Cell Biol* 152: 531–543

Bagde SR & Fromme JC (2022) Structure of a TRAPPII-Rab11 activation intermediate reveals GTPase substrate selection mechanisms. *Sci Adv* 8: eabn7446

Boutté Y, Jonsson K, McFarlane HE, Johnson E, Gendre D, Swarup R, Friml J, Samuels L, Robert S & Bhalerao RP (2013) ECHIDNA-mediated post-Golgi trafficking of auxin carriers for differential cell elongation. *Proc Natl Acad Sci USA* 110: 16259–16264

Brunet S & Sacher M (2014) Are All Multisubunit Tethering Complexes Bona Fide Tethers? *Traffic* 15: 1282–1287

Cai H, Zhang Y, Pypaert M, Walker L & Ferro-Novick S (2005) Mutants in trs120 disrupt traffic from the early endosome to the late Golgi. *J Cell Biol* 171: 823–833

Clark NM, Nolan TM, Wang P, Song G, Montes C, Valentine CT, Guo H, Sozzani R, Yin Y & Walley JW (2021) Integrated omics networks reveal the temporal signaling events of brassinosteroid response in Arabidopsis. *Nat Commun* 12: 5858

Cox J & Mann M (2008) MaxQuant enables high peptide identification rates, individualized p.p.b.-range mass accuracies and proteome-wide protein quantification. *Nat Biotechnol* 26: 1367–1372

Cox J, Neuhauser N, Michalski A, Scheltema RA, Olsen J V. & Mann M (2011) Andromeda: A Peptide Search Engine Integrated into the MaxQuant Environment. *J Proteome Res* 10: 1794–1805

Curtis MD & Grossniklaus U (2003) A Gateway Cloning Vector Set for High-Throughput Functional Analysis of Genes in Planta. *Plant Physiol* 133: 462–469

Dai L, Wang B, Wang T, Meyer EH, Kettel V, Hoffmann N, McFarlane HE, Li S, Wu X, Picard KL, *et al* (2022) The TOR complex controls ATP levels to regulate actin cytoskeleton dynamics in Arabidopsis. *Proc Natl Acad Sci USA* 119: e2122969119

Darwin C (1880) The power of movement in plants London: John Murray

Ding Z, Galván-Ampudia CS, Demarsy E, Łangowski Ł, Kleine-Vehn J, Fan Y, Morita MT, Tasaka M, Fankhauser C, Offringa R, *et al* (2011) Light-mediated polarization of the PIN3 auxin transporter for the phototropic response in Arabidopsis. *Nat Cell Biol* 13: 447–452

Dong L, Wang Z, Liu J & Wang X (2020) AtSK11 and AtSK12 Mediate the Mild Osmotic Stress-Induced Root Growth Response in Arabidopsis. *Int J Mol Sci* 21: 1–16

Elliott L, Moore I & Kirchhelle C (2020) Spatio-temporal control of post-Golgi exocytic trafficking in plants. *J Cell Sci* 133: jcs237065

Friml J, Wiśniewska J, Benková E, Mendgen K & Palme K (2002) Lateral relocation of auxin efflux regulator PIN3 mediates tropism in Arabidopsis. *Nature* 415: 806–809

Galindo A, Planelles-Herrero VJ, Degliesposti G & Munro S (2021) Cryo-EM structure of metazoan TRAPPIII, the multi-subunit complex that activates the GTPase Rab1. *EMBO J* 40: e107608

Garcia VJ, Xu S-L, Ravikumar R, Wang W, Elliott L, Gonzalez E, Fesenko M, Altmann M, Brunschweiger B, Falter-Braun P, *et al* (2020) TRIPP Is a Plant-Specific Component of the Arabidopsis TRAPPII Membrane Trafficking Complex with Important Roles in Plant Development. *Plant Cell* 32: 2424–2443

Garzón PC & Keijzer F (2011) Plants: Adaptive behavior, root-brains, and minimal cognition. *Adapt*

*Behav* 19: 155–171
Gendre D, Jonsson K, Boutté Y & Bhalerao RP (2015) Journey to the cell surface—the central role of the trans-Golgi network in plants. *Protoplasma* 252: 385–398
Gendre D, McFarlane HE, Johnson E, Mouille G, Sjödin A, Oh J, Levesque-Tremblay G, Watanabe Y, Samuels L & Bhalerao RP (2013) Trans-Golgi Network Localized ECHIDNA/Ypt Interacting Protein Complex Is Required for the Secretion of Cell Wall Polysaccharides in Arabidopsis. *Plant Cell* 25: 2633–2646
Gendre D, Oh J, Boutté Y, Best JG, Samuels L, Nilsson R, Uemura T, Marchant A, Bennett MJ, Grebe M, *et al* (2011) Conserved Arabidopsis ECHIDNA protein mediates trans-Golgi-network trafficking and cell elongation. *Proc Natl Acad Sci USA* 108: 8048–8053
González-García M-P, Vilarrasa-Blasi J, Zhiponova M, Divol F, Mora-García S, Russinova E & Caño-Delgado AI (2011) Brassinosteroids control meristem size by promoting cell cycle progression in Arabidopsis roots. *Development* 138: 849–859
Jaber E, Thiele K, Kindzierski V, Loderer C, Rybak K, Jürgens G, Mayer U, Söllner R, Wanner G & Assaad FF (2010) A putative TRAPPII tethering factor is required for cell plate assembly during cytokinesis in Arabidopsis. *New Phytol* 187: 751–763
Jiménez JL, Hegemann B, Hutchins JRA, Peters J-M & Durbin R (2007) A systematic comparative and structural analysis of protein phosphorylation sites based on the mtcPTM database. *Genome Biol* 8: R90
Jumper J, Evans R, Pritzel A, Green T, Figurnov M, Ronneberger O, Tunyasuvunakool K, Bates R, Žídek A, Potapenko A, *et al* (2021) Highly accurate protein structure prediction with AlphaFold. *Nature* 596: 583–589
Kalbfuß N, Strohmayr A, Kegel M, Le L, Grosse-Holz F, Brunschweiger B, Stöckl K, Wiese C, Franke C, Schiestl C, *et al* (2022) A role for brassinosteroid signalling in decision-making processes in the Arabidopsis seedling. *PLoS Genet* 18: e1010541
Kalde M, Elliott L, Ravikumar R, Rybak K, Altmann M, Klaeger S, Wiese C, Abele M, Al B, Kalbfuß N, *et al* (2019) Interactions between Transport Protein Particle (TRAPP) complexes and Rab GTPases in Arabidopsis. *Plant J* 100: 279–297
Karban R & Orrock JL (2018) A judgment and decision-making model for plant behavior. *Ecology* 99: 1909–1919
Kim JJ, Lipatova Z & Segev N (2016) TRAPP Complexes in Secretion and Autophagy. *Front Cell Dev Biol* 4: 20
Kim S-J & Bassham DC (2011) TNO1 Is Involved in Salt Tolerance and Vacuolar Trafficking in Arabidopsis. *Plant Physiol* 156: 514–526
Kim T-W, Michniewicz M, Bergmann DC & Wang Z-Y (2012) Brassinosteroid regulates stomatal development by GSK3-mediated inhibition of a MAPK pathway. *Nature* 482: 419–422
Kim T-W, Park CH, Hsu C-C, Kim Y-W, Ko Y-W, Zhang Z, Zhu J-Y, Hsiao Y-C, Branon T, Kaasik K, *et al* (2023) Mapping the signaling network of BIN2 kinase using TurboID-mediated biotin labeling and phosphoproteomics. *Plant Cell* 35: 975–993
Konstantinova N, Korbei B & Luschnig C (2021) Auxin and Root Gravitropism: Addressing Basic Cellular Processes by Exploiting a Defined Growth Response. *Int J Mol Sci* 22: 2749
Lee C-F, Pu H-Y, Wang L-C, Sayler RJ, Yeh C-H & Wu S-J (2006) Mutation in a homolog of yeast Vps53p accounts for the heat and osmotic hypersensitive phenotypes in Arabidopsis hit1-1 mutant. *Planta* 224: 330–338
Li C, Zhang B & Yu H (2021) GSK3s: nodes of multilayer regulation of plant development and stress responses. *Trends Plant Sci* 26: 1286–1300
Li J & Nam KH (2002) Regulation of Brassinosteroid Signaling by a GSK3/SHAGGY-Like Kinase. *Science* 295: 1299–1301
Li J, Nam KH, Vafeados D & Chory J (2001) BIN2, a New Brassinosteroid-Insensitive Locus in Arabidopsis. *Plant Physiol* 127: 14–22
Liu L, Qin L, Safdar L Bin, Zhao C, Cheng X, Xie M, Zhang Y, Gao F, Bai Z, Huang J, *et al* (2023)

933 The plant trans-Golgi network component ECHIDNA regulates defense, cell death, and
934 endoplasmic reticulum stress. *Plant Physiol* 191: 558–574
935 Lv M & Li J (2020) Molecular Mechanisms of Brassinosteroid-Mediated Responses to Changing
936 Environments in Arabidopsis. *Int J Mol Sci* 21: 2737
937 MacLean B, Tomazela DM, Shulman N, Chambers M, Finney GL, Frewen B, Kern R, Tabb DL,
938 Liebler DC & MacCoss MJ (2010) Skyline: an open source document editor for creating and
939 analyzing targeted proteomics experiments. *Bioinformatics* 26: 966–968
940 McClung CR (2006) Plant Circadian Rhythms. *Plant Cell* 18: 792–803
941 McFarlane HE, Watanabe Y, Gendre D, Carruthers K, Levesque-Tremblay G, Haughn GW,
942 Bhalerao RP & Samuels L (2013) Cell Wall Polysaccharides are Mislocalized to the Vacuole
943 in echidna Mutants. *Plant Cell Physiol* 54: 1867–1880
944 Mi C, Zhang L, Huang G, Shao G, Yang F, You X, Dong M-Q, Sun S & Sui S-F (2022) Structural
945 basis for assembly of TRAPPII complex and specific activation of GTPase Ypt31/32. *Sci Adv*
946 8: eabi5603
947 Morozova N, Liang Y, Tokarev AA, Chen SH, Cox R, Andrejic J, Lipatova Z, Sciorra VA, Emr SD
948 & Segev N (2006) TRAPPII subunits are required for the specificity switch of a Ypt–Rab GEF.
949 *Nat Cell Biol* 8: 1263–1269
950 Naramoto S, Nodzyński T, Dainobu T, Takatsuka H, Okada T, Friml J & Fukuda H (2014) VAN4
951 Encodes a Putative TRS120 That is Required for Normal Cell Growth and Vein Development
952 in Arabidopsis. *Plant Cell Physiol* 55: 750–763
953 Perez-Riverol Y, Csordas A, Bai J, Bernal-Llinares M, Hewapathirana S, Kundu DJ, Inuganti A,
954 Griss J, Mayer G, Eisenacher M, *et al* (2019) The PRIDE database and related tools and
955 resources in 2019: improving support for quantification data. *Nucleic Acids Res* 47: D442–
956 D450
957 Pinar M, Arias-Palomo E, de los Ríos V, Arst HNJ & Peñalva MA (2019) Characterization of
958 Aspergillus nidulans TRAPPs uncovers unprecedented similarities between fungi and
959 metazoans and reveals the modular assembly of TRAPPII. *PLoS Genet* 15: e1008557
960 Pinar M, Arst HN, Pantazopoulou A, Tagua VG, de los Ríos V, Rodríguez-Salarichs J, Díaz JF &
961 Peñalva MA (2015) TRAPPII regulates exocytic Golgi exit by mediating nucleotide exchange
962 on the Ypt31 ortholog RabE$^{RAB11}$. *Proc Natl Acad Sci USA* 112: 4346–4351
963 Pinar M & Peñalva MA (2020) En bloc TGN recruitment of Aspergillus TRAPPII reveals TRAPP
964 maturation as unlikely to drive RAB1-to-RAB11 transition. *J Cell Sci* 133: jcs241141
965 Planas-Riverola A, Gupta A, Betegón-Putze I, Bosch N, Ibañes M & Caño-Delgado AI (2019)
966 Brassinosteroid signaling in plant development and adaptation to stress. *Development* 146:
967 dev151894
968 Pusch S, Harashima H & Schnittger A (2012) Identification of kinase substrates by bimolecular
969 complementation assays. *Plant J* 70: 348–356
970 Qi X, Kaneda M, Chen J, Geitmann A & Zheng H (2011) A specific role for Arabidopsis TRAPPII
971 in post-Golgi trafficking that is crucial for cytokinesis and cell polarity. *Plant J* 68: 234–248
972 Qi X & Zheng H (2011) Arabidopsis TRAPPII is functionally linked to Rab-A, but not Rab-D in polar
973 protein trafficking in trans-Golgi network. *Plant Signal Behav* 6: 1679–1683
974 Ravikumar R, Kalbfuß N, Gendre D, Steiner A, Altmann M, Altmann S, Rybak K, Edelmann H,
975 Stephan F, Lampe M, *et al* (2018) Independent yet overlapping pathways ensure the
976 robustness and responsiveness of trans-Golgi network functions in Arabidopsis.
977 *Development* 145: dev169201
978 Ravikumar R, Steiner A & Assaad FF (2017) Multisubunit tethering complexes in higher plants.
979 *Curr Opin Plant Biol* 40: 97–105
980 Riedel F, Galindo A, Muschalik N & Munro S (2018) The two TRAPP complexes of metazoans
981 have distinct roles and act on different Rab GTPases. *J Cell Biol* 217: 601–617
982 Rosquete MR & Drakakaki G (2018) Plant TGN in the stress response: a compartmentalized
983 overview. *Curr Opin Plant Biol* 46: 122–129

984 Rosquete MR, Worden N, Ren G, Sinclair RM, Pfleger S, Salemi M, Phinney BS, Domozych D,
985 Wilkop T & Drakakaki G (2019) AtTRAPPC11/ROG2: A Role for TRAPPs in Maintenance of
986 the Plant Trans-Golgi Network/Early Endosome Organization and Function. *Plant Cell* 31:
987 1879–1898
988 Rybak K, Steiner A, Synek L, Klaeger S, Kulich I, Facher E, Wanner G, Kuster B, Zarsky V,
989 Persson S, *et al* (2014) Plant Cytokinesis Is Orchestrated by the Sequential Action of the
990 TRAPPII and Exocyst Tethering Complexes. *Dev Cell* 29: 607–620
991 Sambrook J, Fritsch EF & Maniatis T (1989) Molecular Cloning: A Laboratory Manual Cold Spring
992 Harbor Laboratory Press
993 Schwab R, Ossowski S, Riester M, Warthmann N & Weigel D (2006) Highly Specific Gene
994 Silencing by Artificial MicroRNAs in Arabidopsis. *Plant Cell* 18: 1121–1133
995 Seki M, Carninci P, Nishiyama Y, Hayashizaki Y & Shinozaki K (1998) High-efficiency cloning of
996 Arabidopsis full-length cDNA by biotinylated CAP trapper. *Plant J* 15: 707–720
997 Seki M, Narusaka M, Kamiya A, Ishida J, Satou M, Sakurai T, Nakajima M, Enju A, Akiyama K,
998 Oono Y, *et al* (2002) Functional Annotation of a Full-Length Arabidopsis cDNA Collection.
999 *Science* 296: 141–145
1000 Severino LS (2021) Plants make smart decisions in complex environments. *Plant Signal Behav*
1001 16: 1970448
1002 Sharma V, Eckels J, Schilling B, Ludwig C, Jaffe JD, MacCoss MJ & MacLean B (2018) Panorama
1003 Public: A Public Repository for Quantitative Data Sets Processed in Skyline. *Mol Cell*
1004 *Proteomics* 17: 1239–1244
1005 Sharma V, Eckels J, Taylor GK, Shulman NJ, Stergachis AB, Joyner SA, Yan P, Whiteaker JR,
1006 Halusa GN, Schilling B, *et al* (2014) Panorama: A Targeted Proteomics Knowledge Base. *J*
1007 *Proteome Res* 13: 4205–4210
1008 Shevchenko A, Tomas H, Havli J, Olsen J V & Mann M (2006) In-gel digestion for mass
1009 spectrometric characterization of proteins and proteomes. *Nat Protoc* 1: 2856–2860
1010 Söllner R, Glässer G, Wanner G, Somerville CR, Jürgens G & Assaad FF (2002) Cytokinesis-
1011 Defective Mutants of Arabidopsis. *Plant Physiol* 129: 678–690
1012 Song Y, Wang Y, Yu Q, Sun Y, Zhang J, Zhan J & Ren M (2023) Regulatory network of GSK3-
1013 like kinases and their role in plant stress response. *Front Plant Sci* 14: 1123436
1014 Steiner A, Rybak K, Altmann M, McFarlane HE, Klaeger S, Nguyen N, Facher E, Ivakov A, Wanner
1015 G, Kuster B, *et al* (2016) Cell cycle-regulated PLEIADE/AtMAP65-3 links membrane and
1016 microtubule dynamics during plant cytokinesis. *Plant J* 88: 531–541
1017 Swarbreck D, Wilks C, Lamesch P, Berardini TZ, Garcia-Hernandez M, Foerster H, Li D, Meyer
1018 T, Muller R, Ploetz L, *et al* (2008) The Arabidopsis Information Resource (TAIR): gene
1019 structure and function annotation. *Nucleic Acids Res* 36: D1009–D1014
1020 Tang W, Yuan M, Wang R, Yang Y, Wang C, Oses-Prieto JA, Kim T-W, Zhou H-W, Deng Z,
1021 Gampala SS, *et al* (2011) PP2A activates brassinosteroid-responsive gene expression and
1022 plant growth by dephosphorylating BZR1. *Nat Cell Biol* 13: 124–131
1023 Thellmann M, Rybak K, Thiele K, Wanner G & Assaad FF (2010) Tethering Factors Required for
1024 Cytokinesis in Arabidopsis. *Plant Physiol* 154: 720–732
1025 Thomas LL & Fromme JC (2016) GTPase cross talk regulates TRA PPII activation of Rab11
1026 homologues during vesicle biogenesis. *J Cell Biol* 215: 499–513
1027 Truernit E, Bauby H, Dubreucq B, Grandjean O, Runions J, Barthélémy J & Palauqui J-C (2008)
1028 High-Resolution Whole-Mount Imaging of Three-Dimensional Tissue Organization and Gene
1029 Expression Enables the Study of Phloem Development and Structure in Arabidopsis. *Plant*
1030 *Cell* 20: 1494–1503
1031 Tyanova S, Temu T & Cox J (2016a) The MaxQuant computational platform for mass
1032 spectrometry-based shotgun proteomics. *Nat Protoc* 11: 2301–2319
1033 Tyanova S, Temu T, Sinitcyn P, Carlson A, Hein MY, Geiger T, Mann M & Cox J (2016b) The
1034 Perseus computational platform for comprehensive analysis of (prote)omics data. *Nat*

1035 *Methods* 13: 731–740
1036 Uemura T (2016) Physiological Roles of Plant Post-Golgi Transport Pathways in Membrane
1037 Trafficking. *Plant Cell Physiol* 57: 2013–2019
1038 Uemura T, Ueda T & Nakano A (2012) The physiological role of SYP4 in the salinity and osmotic
1039 stress tolerances. *Plant Signal Behav* 7: 1118–1120
1040 Varadi M, Anyango S, Deshpande M, Nair S, Natassia C, Yordanova G, Yuan D, Stroe O, Wood
1041 G, Laydon A, *et al* (2022) AlphaFold Protein Structure Database: massively expanding the
1042 structural coverage of protein-sequence space with high-accuracy models. *Nucleic Acids Res*
1043 50: D439–D444
1044 Vert G & Chory J (2006) Downstream nuclear events in brassinosteroid signalling. *Nature* 441:
1045 96–100
1046 Wang L-C, Tsai M-C, Chang K-Y, Fan Y-S, Yeh C-H & Wu S-J (2011) Involvement of the
1047 Arabidopsis HIT1/AtVPS53 tethering protein homologue in the acclimation of the plasma
1048 membrane to heat stress. *J Exp Bot* 62: 3609–3620
1049 Yan Z, Zhao J, Peng P, Chihara RK & Li J (2009) BIN2 Functions Redundantly with Other
1050 Arabidopsis GSK3-Like Kinases to Regulate Brassinosteroid Signaling. *Plant Physiol* 150:
1051 710–721
1052 Youn J-H & Kim T-W (2015) Functional Insights of Plant GSK3-like Kinases: Multi-Taskers in
1053 Diverse Cellular Signal Transduction Pathways. *Mol Plant* 8: 552–565
1054 Zhao R, Li N, Lin Q, Li M, Shen X, Peng Y, Du Y, Ning Q, Li Y, Zhan J, *et al* (2023) ZmBET5L1
1055 inhibits primary root growth and decreases osmotic stress tolerance by mediating vesicle
1056 aggregation and tethering in maize. *Plant Cell Environ* 46: 975–990
1057 Zhu J, Gong Z, Zhang C, Song C-P, Damsz B, Inan G, Koiwa H, Zhu J-K, Hasegawa PM &
1058 Bressan RA (2002) OSM1/SYP61: A Syntaxin Protein in Arabidopsis Controls Abscisic Acid-
1059 Mediated and Non-Abscisic Acid-Mediated Responses to Abiotic Stress. *Plant Cell* 14: 3009–
1060 3028
1061

1062 **FIGURE LEGENDS**

1063

1064 **Figure 1. The TRAPPII interactome.**

1065 The data are derived from an analysis of IP-MS from inflorescences with the TRAPPII-specific
1066 subunit CLUB:GFP as bait (see Fig. 1B; Kalde *et al*, 2019). Each protein was present in all three
1067 biological replicates. The soluble GFP empty vector was used as a negative control.

1068 **A.** Gene ontology (GO) term enrichment analysis of the TRAPPII interactome. Depicted are highly
1069 enriched (fold enrichment ≥ 4) and significant (FDR-adjusted *P*-value ≤ 0.003) GO term
1070 associations of biological processes of level 0 as bar plots. The length of each bar depicts the fold
1071 enrichment of GO terms associated with detected proteins, while the color intensity indicates the
1072 significance given as the *P*-value adjusted for the false discovery rate (FDR). Interactors of
1073 intermediate intensity (> 5 and < 8) were used (see Fig. S1A for an analysis of high confidence
1074 interactors).

1075 **B, C.** Volcano plots are presented. On the X axis: The ratio (or fold-change) was calculated for
1076 each protein as the average intensity of the signal in the experiment divided by its average
1077 intensity in the control. On the Y axis the *P*-values of the signal in the experiment versus the
1078 control, depicted along a negative log10 scale, are shown. Dotted grey lines represent cutoffs: *P*-
1079 value ≤ 0.02 and Ratio > 8 for high fold-change or > 5 for intermediate fold-change for panel B
1080 and > 1 for panel C. **B.** Note that TRAPPII subunits (light blue for core TRAPP; dark blue for
1081 TRAPPII-specific subunits; the CLUB/AtTRS130:GFP TRAPPII-specific bait is depicted as an
1082 open circle) are in the upper right field, indicating high abundance and good reproducibility. AtSKs
1083 (magenta), MAP65-1 (orange) and RAB-A2a GTPase (green) are all in the upper middle field;
1084 these may be transient interactors of TRAPPII. Note that AtSKs (AtSK11/12/32) are more
1085 significant than validated interactors such as MAP65 and RAB-A2a (Kalde *et al*, 2019; Steiner *et*
1086 *al*, 2016). **C.** Highlighted in magenta are members of the brassinosteroid signaling pathway that
1087 were differentially enriched over light- versus dark-grown seedlings in a different IP-MS
1088 experiment. Note that BSK8, and ROC1 did not meet the significance cutoffs. The most significant
1089 interactors were GSK3/AtSK shaggy-like kinases and TOR. Related to Fig. S1, Table S2.

1090

1091

1092 **Figure 2. GSK3/AtSK sites in TRAPPII and binary interactions.**

1093 Yeast two-hybrid assays were carried out by pairwise one-on-one mating in four independent
1094 replicate experiments, of which three (B) or four (F) are shown. As negative control, the respective

1095 AD constructs were tested with the empty DB vector. The panels are from different plates (in B,
1096 F).
1097 **A.** TRAPPII-specific truncations for yeast two-hybrid were based on phylogenetic analysis (Steiner
1098 *et al*, 2016). Conserved sequences are depicted in red, intermediate degrees of conservation in
1099 orange, and plant-specific sequences are in green. All three GSK3 sites found to be
1100 phosphorylated *in vivo* reside in the plant-specific moiety of TRS120-T2 (green; a blue rectangle
1101 delineates the region of interest).
1102 **B.** Yeast two-hybrid assays of interactions between BIN2 and TRAPPII subunits. BIN2 was fused
1103 to the GAL4 DNA-binding domain (DB) and TRAPPII subunits and truncations thereof (CLUB-C1,
1104 -C2, -C3 and TRS120-T1, -T2, -T3) to the GAL4 activation domain (AD). The results show
1105 interactions between BIN2 and AtTRS120-T2 wild type. BIN2 bound specifically to the TRAPPII
1106 subunit TRS120 and not with other TRAPPII subunits or truncations. In a total of > 2400 pairwise
1107 tests, BIN2 was the only kinase we found that interacted with a TRAPP subunit. The Y2H did not
1108 detect CLUB/AtTRS130-BIN2 interaction shown in Fig. 1B, which shows co-purified proteins that
1109 can include indirect - as opposed to binary - interactors.
1110 **C.** GSK3 sites in AtTRS120-T2. The α-phosphosite of AtTRS120 spans amino acid positions S922
1111 and S923, the β-phosphosite amino acids S971-S975 and the γ-phosphosite amino acid residue
1112 S1165. The canonical GSK3 consensus sequence is: (<u>pS/pT</u>)*XXX*(<u>S/T</u>), and the β-phosphosite
1113 fits this definition (see underlined <u>S</u>XXX<u>S</u>). Even though they are annotated as GSK3 sites in the
1114 PPSP (https://www.phosphosite.org) database, the α-phosphosite deviates somewhat with
1115 <u>S</u>XXXX<u>S</u>, and the γ-phosphosite deviates completely. Amino acids in red were mutated to A or D
1116 via site-directed mutagenesis. Amino acids highlighted in yellow were found to be phosphorylated
1117 *in vivo* (see Fig. S2) and these were all serines.
1118 **D.** The Arabidopsis TRAPPII complex consists of seven shared core subunits (TCA17, TRS33,
1119 BET3, BET5, TRS23, TRS31, TRS20; light blue) and three TRAPPII-specific subunits
1120 (CLUB/AtTRS130, AtTRS120 and the plant-specific subunit TRIPP), and forms a dimer with plant-
1121 specific domains (green) at the predicted dimer interface (Kalde *et al*, 2019; Garcia *et al*, 2020).
1122 This model is based on extensive pair-wise yeast two-hybrid analysis between TRAPPII subunits
1123 in *Arabidopsis* (Kalde *et al*, 2019; Garcia *et al*, 2020).
1124 **E.** Mapping of GSK3/AtSK sites on an AlphaFold structural prediction (Jumper *et al*, 2021; Varadi
1125 *et al*, 2022) of AtTRS120. A lateral view and a frontal perspective are shown. Note that all three
1126 GSK3/AtSK sites (magenta sticks) reside in unstructured, flexible and accessible regions of the
1127 protein.

1128 **F.** Interactions between BIN2 and TRAPPII complex subunits (CLUB-C2, CLUB-C3, TRS120-T1,
1129 TRS120-T3 truncations), as positive controls, fused to the GAL4 DNA-binding domain (DB) and
1130 TRS120-T2 truncation and its phosphomutants TRS120-T2 SαD, SβD, SγD, SαβD and SαβγD
1131 fused to the GAL4 activation domain (AD). Note the positive interactions between BIN2 and
1132 AtTRS120-T2 wild type and phosphovariants; there was, however, no reproducible interaction if
1133 all three target sites were phosphomimetic (TRS120-T2 SαβγD). Related to Fig. S2-S4.
1134
1135
1136 **Figure 3. *In vitro* AtSK kinase assays with TRS120 as bait.**
1137 **A.** *In vitro* kinase assays using GST:AtBIN2 (69 kDa) and GST:TRS120-T2 (100 kDa). The change
1138 of phosphosignal is shown in a representative autoradiograph (upper panel) and the loaded
1139 protein amount in the corresponding CBB (Coomassie stain, lower panel). Non-phosphorylatable
1140 S to A TRS120-T2 variants were used as negative controls. The means ± SD of phosphosignals
1141 were normalized to the protein amount and related to non-mutated TRS120-T2 wild-type control.
1142 Note that BIN2 phosphorylated AtTRS120-T2 *in vitro,* with a preference for wild-type (WT)
1143 sequences over non-phosphorylatable AtTRS120-SγA, AtTRS120-SαγA, AtTRS120-SβγA and
1144 AtTRS120-SαβγA substrates. n = 3 independent experiments; *: $P<0.05$ for significant differences
1145 to TRS120-T2 WT (set at 1.0 right panel) determined by using a one sample two-tailed t-test.
1146 **B.** Kinase assays were performed *in vitro* with mass-spectrometry readout. One member of each
1147 shaggy-like kinase clade (AtSKs; see Fig. S3A) was used with the TRS120-T2 truncation as
1148 substrate. Dilution series of the kinase are depicted in different shades of blue. AtTRS120-T2 has
1149 highly (red) and moderately (orange) conserved sequences, as well as plant-specific sequences
1150 (green). Three GSK3 sites (referred to as α, β, γ; see Fig. 2C) can be found in the plant-specific
1151 T2 domain. AtSKs in clades I-III differentially phosphorylated the substrate at three GSK3
1152 consensus sites (with a preference for the γ site) in a time-dependent and concentration-
1153 dependent manner. A clade IV AtSK did not phosphorylate at all. Samples incubated for 120 min
1154 in a kinase buffer without ATP, or samples in which the kinase was heat inactivated (KD), served
1155 as negative controls. The numbers in grey in each plot denote the number of times the
1156 phosphorylation event was seen in the given number of independent replicates. Note the higher
1157 intensity of the TRS120-γ peptide, especially for Clade I/SK11 (1e8 for TRS120-γ versus 1e6 for
1158 TRS120-α and TRS120-β on the Y axis). Related to Fig. S2-S6.
1159
1160

1161 **Figure 4. Role of the TRAPPII complex versus ECHIDNA in hypocotyl/root trade-offs.**
1162 Seedlings were germinated on ½ MS in the dark (dark) or in dark with -0.4 MPa water stress
1163 (darkW). **A.** Col-0 (wild type). **B.** BR signaling mutant *bin2-3bil1bil2* triple knockout (from Kalbfuß
1164 *et al*, 2022). **C.** *club-2*, a null *trappii* mutant. **D.** *trs120-4*, a null *trappii* allele. **E.** *echidna* null allele,
1165 impaired in TGN structure and function. At least 3 experiments were performed for each line, and
1166 a representative one is shown here on the basis of RQ and *P*-values. **F.** Representative seedling
1167 images of Col-0 (wild type) and mutants shown in A-E. *bin2-3bil1bil2* and *trs120-4* mutants failed
1168 to correctly adjust their hypocotyl and root lengths from dark to darkW conditions. Dotted lines
1169 mark the hypocotyl-root junction, whereas arrows point to the end of the root. Scale bar is 1 cm.
1170 **G.** Normalized response quotient $RQ_{ratio}$. Each replicate is represented by a dot. A value of 1
1171 (vertical red line) corresponds to an identical adaptation to darkW conditions as the wild type**.** Note
1172 that the triple *bin2-3bil1bil2* knock out, *trs120-4* and *club-2* had attenuated responses (magenta
1173 arrows). **H.** Volcano plot with the mean $RQ_{ratio}$ depicted on the X axis and the median *P*-value of
1174 the response on the Y axis (negative log scale; a median of all replicates was used). The area
1175 shaded in grey on the red line (green arrow) is where wild-type ecotypes would theoretically map
1176 onto the plot. Mutants in the lower left quadrant (peach shading) were considered to have a
1177 "confused decision phenotype" (see text). *trs120-4* mutants mapped to the lower left quadrant and
1178 qualified as decision mutants on two counts: (i) a consistently opposite hypocotyl response (red
1179 asterisk in D), (ii) failure to adjust the hypocotyl/root ratio to darkW (the ratio for darkW is the same
1180 as for dark in panel D), translating into a non-significant *P*-value for the ratio response (H). The
1181 number (n) of seedlings measured per condition is in grey below the mean ± SD bar graphs. *P*-
1182 values were computed with a two-tailed student's t-test and are represented as follows: *: P<0.05;
1183 **: P<0.01; ***: P<0.001; ****: P<0.0001; *****: P<0.00001. Mutant alleles and the corresponding
1184 ecotypes are described in Table S1. Related to Fig. S8-S9.
1185
1186
1187 **Figure 5. Cellular growth parameters of *trappii* mutants under single versus additive stress**
1188 **conditions.**
1189 Seedlings were grown in the light (orange), dark (black) or dark with -0.4 MPa water stress (darkW;
1190 blue).
1191 **A, B.** Scanning electron micrographs (SEM) of hypocotyls of A) Col-0 wild type and B) *trs120-4,*
1192 null *trappii* allele*.* The cell surface area was calculated as the product of cell width and length.
1193 *trs120-4* mutants showed the opposite hypocotyl cell height and cell surface adaptations to dark-
1194 to-darkW conditions (red asterisks in B) than the wild-type control. Representative SEM images

1195 of seedlings grown under the specified conditions are shown (scale bar = 40 µm). Outlines of
1196 representative cells are highlighted by white dashed lines. Shown are means ± SD. *P*-values were
1197 computed with a two-tailed student's t-test and are represented as follows: ***: P<0.001; ****:
1198 P<0.0001; *****: P<0.00001.
1199 **C, D.** Confocal micrographs of mPS-PI stained C) Col-0 wild type and D) *trs120-4* null mutant root
1200 tips under different environmental conditions; black arrowheads mark the junction between the
1201 meristematic and elongation zones. 10 days after incubation, the cell lengths were measured in
1202 single cortex cell files, starting at the cortex/endodermis initials. Cell lengths of consecutive cells
1203 were mapped as a function of cell number from the quiescent centre (QC). The fitted lines were
1204 generated with Local Polynomial Regression Fitting with the 'loess' method in R; grey shading
1205 designates the 95 percent confidence interval. Col-0 seedlings grown in the dark with and without
1206 water stress show steep slopes (green arrows). In the *trappii* mutant the curves exhibit a minimal
1207 to no difference between the different screen conditions (magenta arrows). Scale bar is 50 µm.
1208 The sample size (n) is given in each panel as the number of cells/ number of seedlings that were
1209 analyzed (A-D). Related to Fig. S11.
1210
1211
1212 **Figure 6. Responses of TRS120 phosphovariants to osmotic or additive stress.**
1213 Phosphovariants of $P_{TRS120}$::TRS120:GFP (Rybak *et al*, 2014) were in *trs120-4* homozygous
1214 backgrounds with the exception of the TRS120-SαβγD variant in panels A-C, which was in a
1215 hemizygous *trs120-4*/+ background.
1216 **A-C.** Germination of TRS120 phosphovariants under osmotic stress**.** Effect of A) 0 mM, B) 200
1217 mM and C) 400 mM mannitol on seed germination of the TRS120-SαβγA, the TRS120-SαβγD
1218 mutants and the following controls: Col-0 wild type; the ABA deficient mutant *aba2-1* and the ABA
1219 PP2C coreceptor triple knock-out line *hab1-1 abi1-2 pp2ca-1*. The non-phosphorylatable TRS120-
1220 SαβγA mutation increased seed germination on higher mannitol concentrations, whereas the
1221 phosphomimetic TRS120-SαβγD decreased seed germination. Shown are the means ± SD of
1222 three technical replicates. Similar results were obtained in three independent biological replicates.
1223 Stars indicate statistical significance compared to the wild-type Col-0 calculated with a two-tailed
1224 student's t-test (*: P<0.05; **: P<0.01; ***: P<0.001; ****: P<0.0001). DAS: days after stratification.
1225 **D-F**. Response quotients (RQ) of D) the hypocotyl, E) the root and F) the hypocotyl/root ratio of
1226 the non-phosphorylatable TRS120-SαβγA and the phosphomimetic TRS120-SαβγD mutants for
1227 dark-to-dark with water stress (-0.4 MPa, darkW) adaptation. The divergent hypocotyl and root
1228 responses of TRS120-SαβγA and TRS120-SαβγD mutants resulted in a strong hypocotyl/root

1229 ratio phenotype under darkW conditions compared to the TRS120-WT control. TRS120-SαβγA
1230 showed an enhanced ratio adaption, whereas TRS120-SαβγD mutants had an attenuated ratio
1231 response. RQ response quotients are normalized to the rescue mutant TRS120-WT
1232 ($P_{TRS120}$::TRS120:GFP in *trs120-4/trs120-4*). A value of 1 (vertical red line) corresponds to an
1233 identical adaptation to darkW conditions as the rescue mutant. Note that due to the opposite
1234 adaptations of the hypocotyl and root under the additive stress conditions (decrease in hypocotyl
1235 and increase in root length from dark-to-darkW), the respective thresholds for attenuated and
1236 enhanced responses are opposite. Dots represent biological replicates, of which there were a total
1237 of four primary transformants per line. Mean RQ values are given on the right. Related to Fig. S14-
1238 S15.
1239
1240
1241 **Figure 7. Genetic interaction between *bin2* higher order and *trappii* conditional mutants**
1242 Seedlings were transferred to estradiol (Est; induced) or EtOH (mock) containing media and grown
1243 vertically for 9 days.
1244 **A.** A conditional *trs120* knock-down allele, *trs120i*. This features an artificial microRNA targeting
1245 the 5' end of the AtTRS120/TRAPPC9 coding sequence, expressed under an estradiol-inducible
1246 promoter. LB: left border; RB: right border; G10-90: synthetic constitutive promoter; XVE: encoding
1247 a chimeric transcription factor composed of the DNA-binding domain of the bacterial repressor
1248 LexA (X), the acidic transactivating domain of VP16 (V) and the regulatory region of the human
1249 estrogen receptor (E); T3A: poly(A) addition sequence; HygR: hygromycin resistance marker;
1250 OlexA-46: estradiol inducible promoter system with multiple copies of the lexA binding domain.
1251 **B.** Representative seedling images of Col-0 (wild type), *trs120i* mutant, *bin2-3bil1bil2* and *bin2-*
1252 *3bil1bil2 trs120i* higher order mutants grown on estradiol. Upon induction, *trs120i* exhibited a mild
1253 phenotype, with a wavy primary root, and *bin2-3bil1bil2* a more pronounced root agravitropism. In
1254 contrast, *bin2-3bil1bil2 trs120i* mutants had an enhanced root agravitropism, growing against
1255 gravity or in loops (yellow arrow points to a 360° loop in the primary root). Scale bar is 1 cm.
1256 **C.** Visualisation of the primary root growth orientation. Primary root tip angles (excluding lateral
1257 roots) of Col-0, *trs120i*, *bin2-3bil1bil2* and *bin2-3bil1bil2 trs120i* seedlings grown on Est were
1258 measured and a frequency count with a bin width of 20° was performed. Frequency plots were
1259 generated by using a polar coordinate system. A root tip angle of 0° corresponds to vertical root
1260 tip growth in line with the gravitropic vector. Primary roots exhibiting looping (see yellow arrow in
1261 B) were scored as -180° due to their growth against gravity. A representative plot for each
1262 genotype is shown.

1263 **D, E.** Quantification of the frequency of agravitropic primary roots upon growth on D) mock (EtOH)
1264 or E) induced (Est) conditions. Frequency of primary root tips growing against gravity (angles < -
1265 90° and > 90° in panel C) was counted per experiment. The *bin2-3bil1bil2 trs120i* higher order
1266 mutant had a more than additively enhanced agravitropic response upon induction as compared
1267 to *trs120i* or *bin2-3bil1bil2* alone (E). Note the synthetic enhancement specifically upon estradiol
1268 induction and not in the mock control (Fig. 7D, compared to 7E). This is indicative of a synergistic
1269 genetic interaction. Mean ± SD bar graphs; **: P≤0.01 two-tailed student's t-test. n = 2 independent
1270 experiments for Col-0 and *bin2-3bil1bil2*, n = 4 for *bin2-3bil1bil2 trs120i* and n = 6 for *trs120i* with
1271 at least 11 seedlings per experiment.
1272
1273
1274 **Figure 8. Flow diagram suggesting how BIN2 might mediate plant adaptive responses by**
1275 **phosphorylating the TRAPPII complex.**
1276 Shaggy-like kinases such as BIN2 integrate a vast number of signaling pathways and, together
1277 with receptor complexes at the cell surface, comprise a surveillance system fine-tuned to both
1278 biotic and abiotic cues (see text for further detail). BIN2 resides at the plasma membrane (PM)
1279 and in the cytosol and TRAPPII resides at the cytosol and in the TGN (Vert & Chory, 2006; Qi *et*
1280 *al*, 2011; Naramoto *et al*, 2014; Rybak *et al*, 2014; Ravikumar *et al*, 2018). We propose that, in the
1281 cytosol, the BIN2-TRAPPII interaction serves in the relay of information from the PM to the TGN.
1282 We posit that signal integration and decision-making occur at the AtSK-TRAPPII interface. A
1283 surface view of the AtTRAPPII complex with AtTRS120 GSK3 phosphorylation sites facing the
1284 predicted active site chamber is depicted as AlphaFold structures of AtTRS120/TRAPPC9 and
1285 CLUB/AtTRS130/TRAPPC10 mapped onto the cryo-EM-generated structures of yeast TRAPPII
1286 (Mi *et al*, 2022; see Fig. S4 for a cross-kingdom structural alignment). Downstream of TRAPPII,
1287 Rab GTPase cascades are postulated to be implicated in implementing decisions reached by the
1288 AtSK-TRAPPII module. We speculate that the phosphorylation status of AtTRS120 modulates the
1289 specificity of the putative TRAPPPII GEF activity, thereby differentially activating distinct Rab
1290 GTPase cascades.
1291 In the lower panel, we show one example of an adaptive growth decision in 10-day-old seedlings
1292 (Col-0 wild type). Bar plots depict hypocotyl (green) versus root (beige-brown) lengths. Light: light-
1293 grown seedling with a short hypocotyl and a long root. Dark: a seedling germinated in the dark
1294 with a long hypocotyl and a short root. DarkW: Water deprivation in the dark; the hypocotyl is
1295 shorter and the root longer than under dark conditions. The dotted green arrow (dark, darkW)
1296 represents the incentive for hypocotyl elongation in search of light and the brown arrow (darkW)

the incentive for root growth in search of water. Thus, darkW is a “conflict of interest” scenario in which hypocotyl and root growth have competing interests (Kalbfuß *et al*, 2022). Figure generated with BioRender.

1301 **SUPPORTING INFORMATION**

1302

1303 **Figure S1.** GO term enrichment and selected brassinosteroid signaling components in IP-MS
1304 with the TRAPPII-specific CLUB:GFP subunit as bait.
1305 **Figure S2.** Fragment ion mass spectra of AtTRS120 phosphopeptides found in
1306 AtTRS120:GFP IP-MS.
1307 **Figure S3.** Fragment ion mass spectra of AtSK/GSK3 kinases found in AtTRS120:GFP IP-
1308 MS.
1309 **Figure S4.** Cross-kingdom structural alignment of TRAPPII.
1310 **Figure S5.** AtSK11 and BIN2 phosphorylate AtTRS120: *in vitro* kinase assays.
1311 **Figure S6.** Pharmacological inhibition or enhancement of TRAPPII phosphorylation by AtSKs
1312 *in vivo*.
1313 **Figure S7.** Cytokinesis and protein sorting in *bin2-1*.
1314 **Figure S8.** Response to single versus additive stress: violin plots.
1315 **Figure S9.** Response to additive stress: response quotients and volcano plots for the
1316 hypocotyl and root.
1317 **Figure S10.** Light responses in *bin2-3bil1bil2*, *trappii* and *echidna* mutants.
1318 **Figure S11.** Cellular hypocotyl parameters of *trappii* mutants under single and additive stress
1319 conditions.
1320 **Figure S12.** Characterization of TRS120:GFP phosphovariants.
1321 **Figure S13.** Localization of TRS120:GFP phosphovariants.
1322 **Figure S14.** The etiolation response in TRS120 phosphovariants.
1323 **Figure S15.** Role of TRS120 phosphorylation status on adaptive growth responses under
1324 additive stress conditions.
1325 **Movie S1.** 3D projection of cross-kingdom structural alignment of TRAPPII.
1326 **Table S1.** Mutant lines used in this study.
1327 **Table S2.** Selected brassinosteroid signaling proteins in the CLUB interactome.
1328 **Table S3.** Thresholds for attenuated, normal and enhanced response quotients.
1329 **Supporting Methods.**

1330

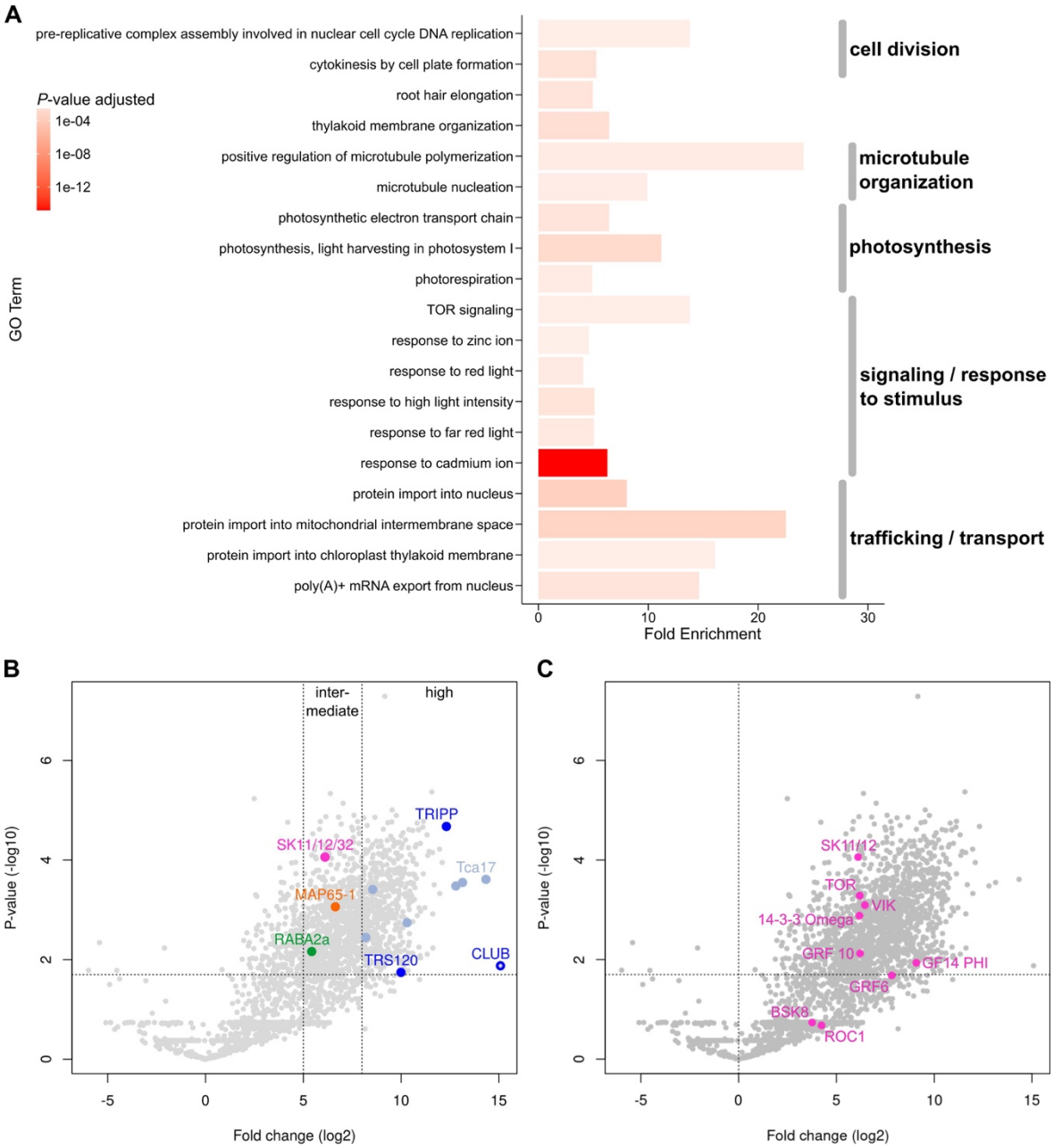


**Figure 1. The TRAPPII interactome.**

The data are derived from an analysis of IP-MS from inflorescences with the TRAPPII-specific subunit CLUB:GFP as bait (see Fig. 1B; Kalde *et al*, 2019). Each protein was present in all three biological replicates. The soluble GFP empty vector was used as a negative control.

**A.** Gene ontology (GO) term enrichment analysis of the TRAPPII interactome. Depicted are highly enriched (fold enrichment ≥ 4) and significant (FDR-adjusted *P*-value ≤ 0.003) GO term associations of biological processes of level 0 as bar plots. The length of each bar depicts the fold enrichment of GO terms associated with detected proteins, while the color intensity indicates the significance given as the *P*-value adjusted for the false discovery rate (FDR). Interactors of intermediate intensity (> 5 and < 8) were used (see Fig. S1A for an analysis of high confidence interactors).

**B, C.** Volcano plots are presented. On the X axis: The ratio (or fold-change) was calculated for each protein as the average intensity of the signal in the experiment divided by its average intensity in the control. On the Y axis the *P*-values of the signal in the experiment versus the control, depicted along a negative log10 scale, are shown. Dotted grey lines represent cutoffs: *P*-value ≤ 0.02 and Ratio > 8 for high fold-change or

> 5 for intermediate fold-change for panel B and > 1 for panel C. **B.** Note that TRAPPII subunits (light blue for core TRAPP; dark blue for TRAPPII-specific subunits; the CLUB/AtTRS130:GFP TRAPPII-specific bait is depicted as an open circle) are in the upper right field, indicating high abundance and good reproducibility. AtSKs (magenta), MAP65-1 (orange) and RAB-A2a GTPase (green) are all in the upper middle field; these may be transient interactors of TRAPPII. Note that AtSKs (AtSK11/12/32) are more significant than validated interactors such as MAP65 and RAB-A2a (Kalde *et al*, 2019; Steiner *et al*, 2016). **C.** Highlighted in magenta are members of the brassinosteroid signaling pathway that were differentially enriched over light- versus dark-grown seedlings in a different IP-MS experiment. Note that BSK8, and ROC1 did not meet the significance cutoffs. The most significant interactors were GSK3/AtSK shaggy-like kinases and TOR. Related to Fig. S1, Table S2.

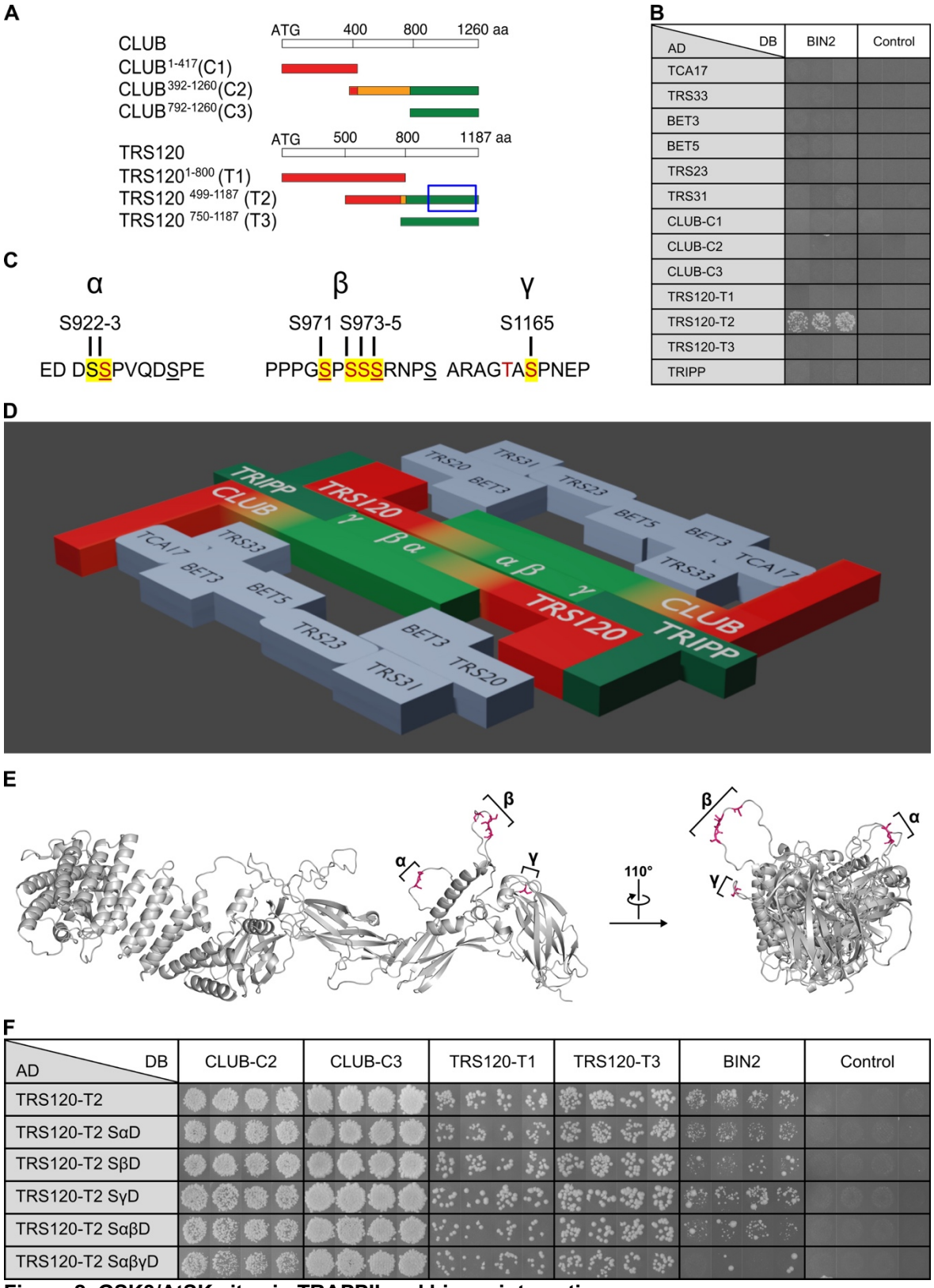


**Figure 2. GSK3/AtSK sites in TRAPPII and binary interactions.**
Yeast two-hybrid assays were carried out by pairwise one-on-one mating in four independent replicate experiments, of which three (B) or four (F) are shown. As negative control, the respective AD constructs were tested with the empty DB vector. The panels are from different plates (in B, F).

**A.** TRAPPII-specific truncations for yeast two-hybrid were based on phylogenetic analysis (Steiner *et al*, 2016). Conserved sequences are depicted in red, intermediate degrees of conservation in orange, and plant-specific sequences are in green. All three GSK3 sites found to be phosphorylated *in vivo* reside in the plant-specific moiety of TRS120-T2 (green; a blue rectangle delineates the region of interest).
**B.** Yeast two-hybrid assays of interactions between BIN2 and TRAPPII subunits. BIN2 was fused to the GAL4 DNA-binding domain (DB) and TRAPPII subunits and truncations thereof (CLUB-C1, -C2, -C3 and TRS120-T1, -T2, -T3) to the GAL4 activation domain (AD). The results show interactions between BIN2 and AtTRS120-T2 wild type. BIN2 bound specifically to the TRAPPII subunit TRS120 and not with other TRAPPII subunits or truncations. In a total of > 2400 pairwise tests, BIN2 was the only kinase we found that interacted with a TRAPP subunit. The Y2H did not detect CLUB/AtTRS130-BIN2 interaction shown in Fig. 1B, which shows co-purified proteins that can include indirect - as opposed to binary - interactors.
**C.** GSK3 sites in AtTRS120-T2. The α-phosphosite of AtTRS120 spans amino acid positions S922 and S923, the β-phosphosite amino acids S971-S975 and the γ-phosphosite amino acid residue S1165. The canonical GSK3 consensus sequence is: (pS/pT)*XXX*(S/T), and the β-phosphosite fits this definition (see underlined SXXXS). Even though they are annotated as GSK3 sites in the PPSP (https://www.phosphosite.org) database, the α-phosphosite deviates somewhat with SXXXXS, and the γ-phosphosite deviates completely. Amino acids in red were mutated to A or D via site-directed mutagenesis. Amino acids highlighted in yellow were found to be phosphorylated *in vivo* (see Fig. S2) and these were all serines.
**D.** The Arabidopsis TRAPPII complex consists of seven shared core subunits (TCA17, TRS33, BET3, BET5, TRS23, TRS31, TRS20; light blue) and three TRAPPII-specific subunits (CLUB/AtTRS130, AtTRS120 and the plant-specific subunit TRIPP), and forms a dimer with plant-specific domains (green) at the predicted dimer interface (Kalde *et al*, 2019; Garcia *et al*, 2020). This model is based on extensive pair-wise yeast two-hybrid analysis between TRAPPII subunits in *Arabidopsis* (Kalde *et al*, 2019; Garcia *et al*, 2020).
**E.** Mapping of GSK3/AtSK sites on an AlphaFold structural prediction (Jumper *et al*, 2021; Varadi *et al*, 2022) of AtTRS120. A lateral view and a frontal perspective are shown. Note that all three GSK3/AtSK sites (magenta sticks) reside in unstructured, flexible and accessible regions of the protein.
**F.** Interactions between BIN2 and TRAPPII complex subunits (CLUB-C2, CLUB-C3, TRS120-T1, TRS120-T3 truncations), as positive controls, fused to the GAL4 DNA-binding domain (DB) and TRS120-T2 truncation and its phosphomutants TRS120-T2 SαD, SβD, SγD, SαβD and SαβγD fused to the GAL4 activation domain (AD). Note the positive interactions between BIN2 and AtTRS120-T2 wild type and phosphovariants; there was, however, no reproducible interaction if all three target sites were phosphomimetic (TRS120-T2 SαβγD). Related to Fig. S2-S4.

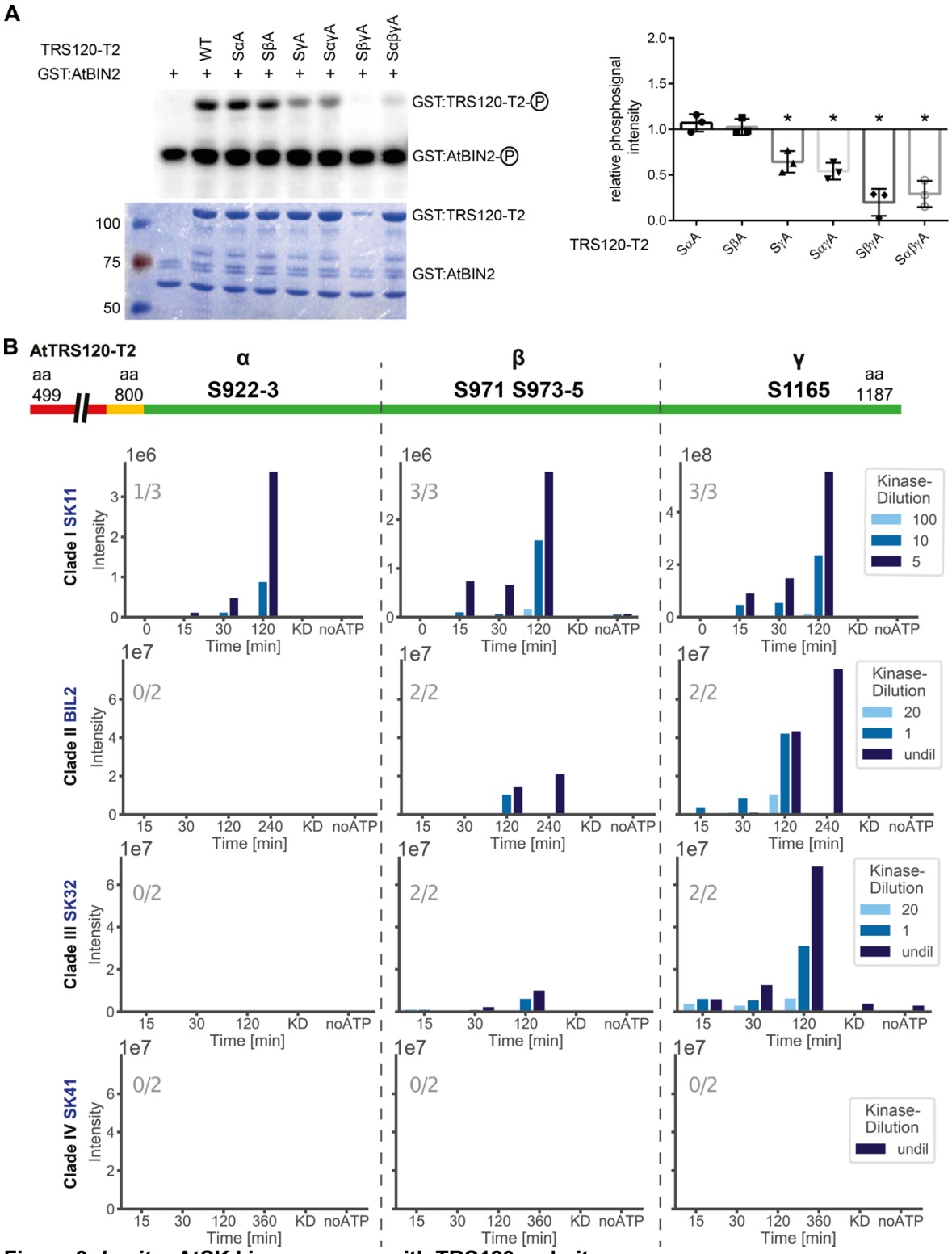


**Figure 3. *In vitro* AtSK kinase assays with TRS120 as bait.**

**A.** *In vitro* kinase assays using GST:AtBIN2 (69 kDa) and GST:TRS120-T2 (100 kDa). The change of phosphosignal is shown in a representative autoradiograph (upper panel) and the loaded protein amount in the corresponding CBB (Coomassie stain, lower panel). Non-phosphorylatable S to A TRS120-T2 variants were used as negative controls. The means ± SD of phosphosignals were normalized to the protein amount and related to non-mutated TRS120-T2 wild-type control. Note that BIN2 phosphorylated AtTRS120-T2 *in*

*vitro,* with a preference for wild-type (WT) sequences over non-phosphorylatable AtTRS120-SγA, AtTRS120-SαγA, AtTRS120-SβγA and AtTRS120-SαβγA substrates. n = 3 independent experiments; *: P<0.05 for significant differences to TRS120-T2 WT (set at 1.0 right panel) determined by using a one sample two-tailed t-test.

**B.** Kinase assays were performed *in vitro* with mass-spectrometry readout. One member of each shaggy-like kinase clade (AtSKs; see Fig. S3A) was used with the TRS120-T2 truncation as substrate. Dilution series of the kinase are depicted in different shades of blue. AtTRS120-T2 has highly (red) and moderately (orange) conserved sequences, as well as plant-specific sequences (green). Three GSK3 sites (referred to as α, β, γ; see Fig. 2C) can be found in the plant-specific T2 domain. AtSKs in clades I-III differentially phosphorylated the substrate at three GSK3 consensus sites (with a preference for the γ site) in a time-dependent and concentration-dependent manner. A clade IV AtSK did not phosphorylate at all. Samples incubated for 120 min in a kinase buffer without ATP, or samples in which the kinase was heat inactivated (KD), served as negative controls. The numbers in grey in each plot denote the number of times the phosphorylation event was seen in the given number of independent replicates. Note the higher intensity of the TRS120-γ peptide, especially for Clade I/SK11 (1e8 for TRS120-γ versus 1e6 for TRS120-α and TRS120-β on the Y axis). Related to Fig. S2-S6.

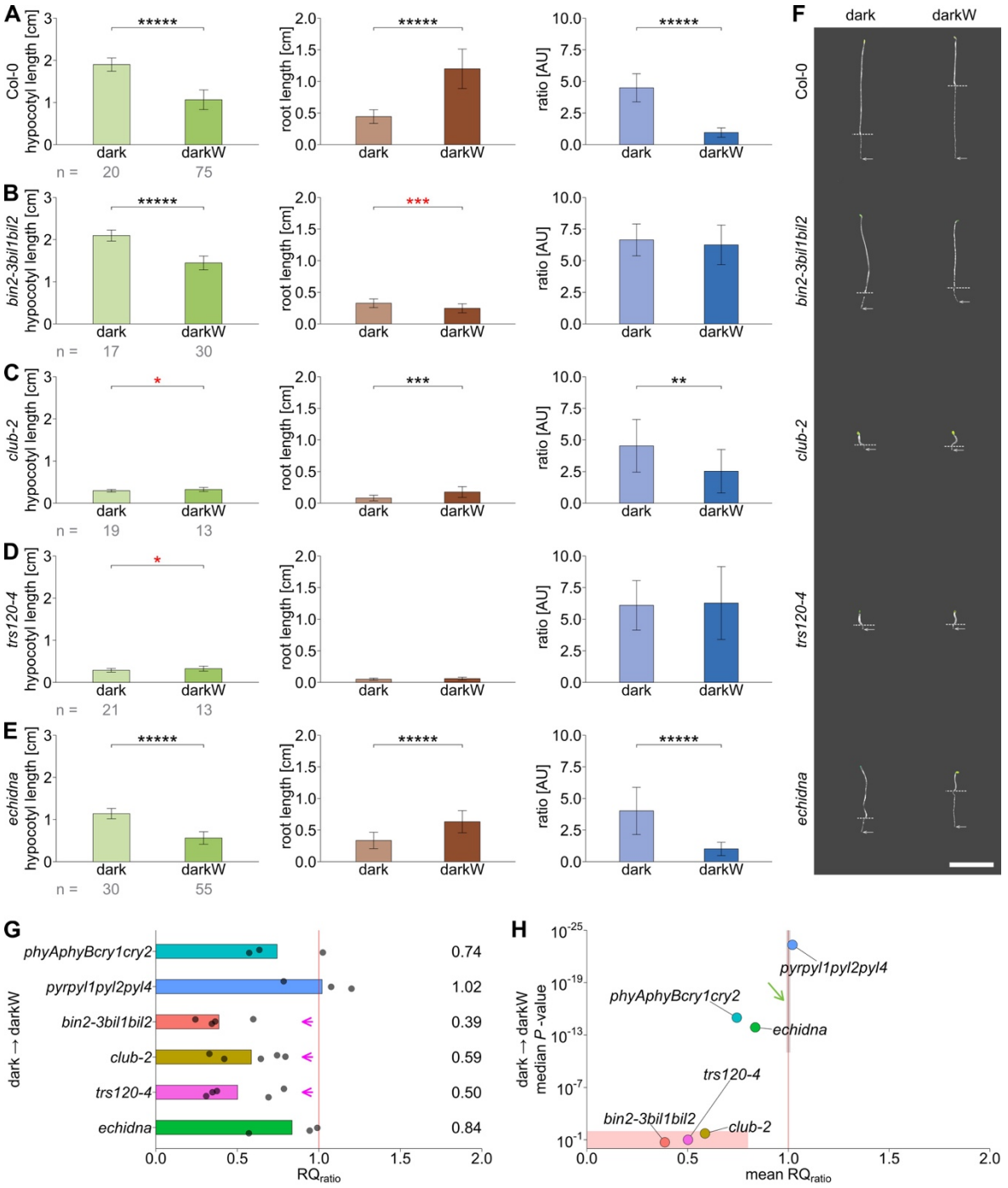


**Figure 4. Role of the TRAPPII complex versus ECHIDNA in hypocotyl/root trade-offs.**
Seedlings were germinated on ½ MS in the dark (dark) or in dark with -0.4 MPa water stress (darkW). **A.** Col-0 (wild type). **B.** BR signaling mutant *bin2-3bil1bil2* triple knockout (from Kalbfuß *et al*, 2022). **C.** *club-2*, a null *trappii* mutant. **D.** *trs120-4*, a null *trappii* allele. **E.** *echidna* null allele, impaired in TGN structure and function. At least 3 experiments were performed for each line, and a representative one is shown here on the basis of RQ and *P*-values. **F.** Representative seedling images of Col-0 (wild type) and mutants shown in A-E. *bin2-3bil1bil2* and *trs120-4* mutants failed to correctly adjust their hypocotyl and root lengths from dark to darkW conditions. Dotted lines mark the hypocotyl-root junction, whereas arrows point to the end of the root. Scale bar is 1 cm. **G.** Normalized response quotient $RQ_{ratio}$. Each replicate is represented by a dot. A value of 1 (vertical red line) corresponds to an identical adaptation to darkW conditions as the wild type**.** Note that the triple *bin2-3bil1bil2* knock out, *trs120-4* and *club-2* had attenuated responses (magenta

arrows). **H.** Volcano plot with the mean $RQ_{ratio}$ depicted on the X axis and the median *P*-value of the response on the Y axis (negative log scale; a median of all replicates was used). The area shaded in grey on the red line (green arrow) is where wild-type ecotypes would theoretically map onto the plot. Mutants in the lower left quadrant (peach shading) were considered to have a "confused decision phenotype" (see text). *trs120-4* mutants mapped to the lower left quadrant and qualified as decision mutants on two counts: (i) a consistently opposite hypocotyl response (red asterisk in D), (ii) failure to adjust the hypocotyl/root ratio to darkW (the ratio for darkW is the same as for dark in panel D), translating into a non-significant *P*-value for the ratio response (H). The number (n) of seedlings measured per condition is in grey below the mean ± SD bar graphs. *P*-values were computed with a two-tailed student's t-test and are represented as follows: *: P<0.05; **: P<0.01; ***: P<0.001; ****: P<0.0001; *****: P<0.00001. Mutant alleles and the corresponding ecotypes are described in Table S1. Related to Fig. S8-S9.

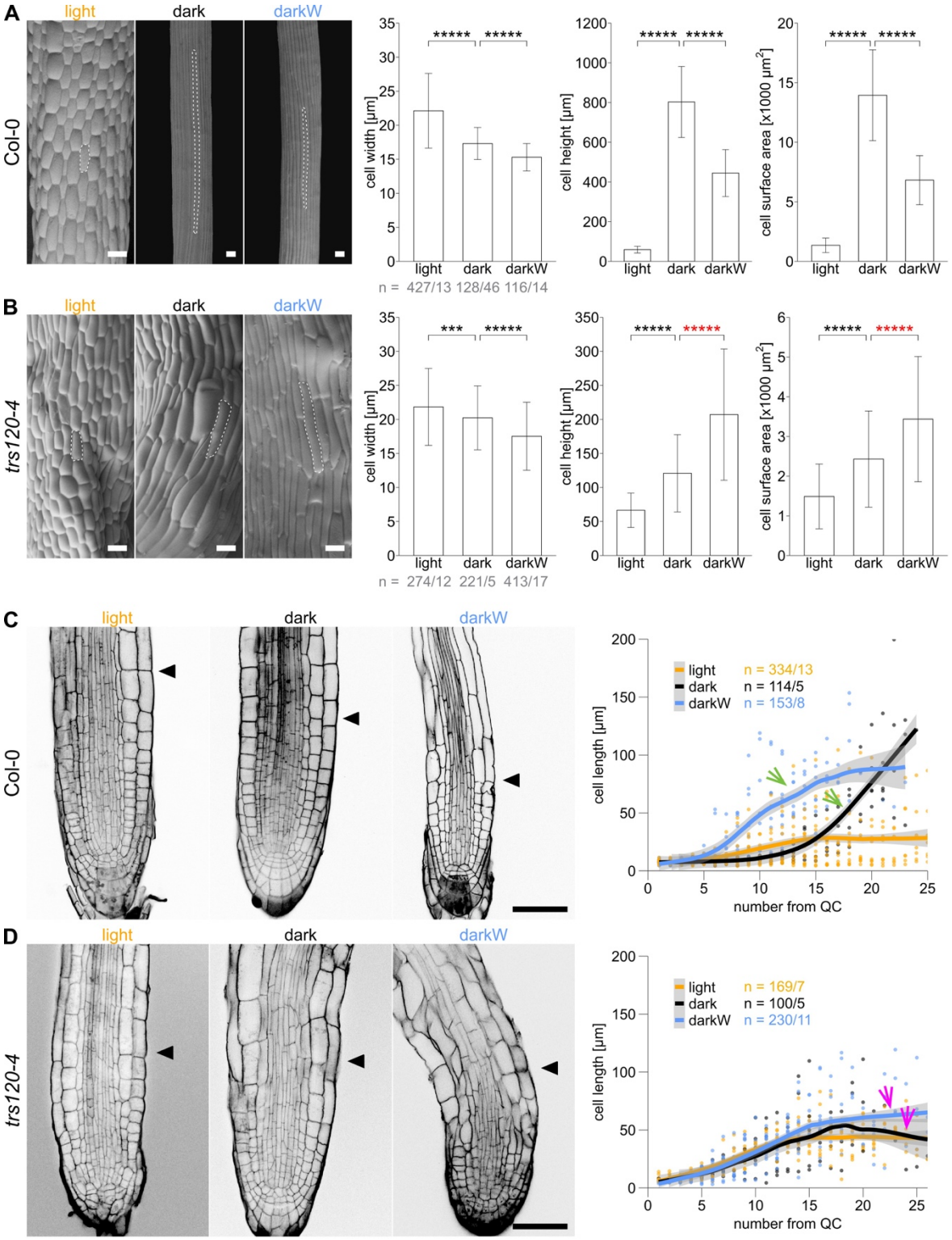


**Figure 5. Cellular growth parameters of *trappii* mutants under single versus additive stress conditions.**

Seedlings were grown in the light (orange), dark (black) or dark with -0.4 MPa water stress (darkW; blue). **A, B.** Scanning electron micrographs (SEM) of hypocotyls of A) Col-0 wild type and B) *trs120-4,* null *trappii* allele. The cell surface area was calculated as the product of cell width and length. *trs120-4* mutants showed the opposite hypocotyl cell height and cell surface adaptations to dark-to-darkW conditions (red asterisks in

B) than the wild-type control. Representative SEM images of seedlings grown under the specified conditions are shown (scale bar = 40 µm). Outlines of representative cells are highlighted by white dashed lines. Shown are means ± SD. *P*-values were computed with a two-tailed student's t-test and are represented as follows: ***: P<0.001; ****: P<0.0001; *****: P<0.00001.

**C, D.** Confocal micrographs of mPS-PI stained C) Col-0 wild type and D) *trs120-4* null mutant root tips under different environmental conditions; black arrowheads mark the junction between the meristematic and elongation zones. 10 days after incubation, the cell lengths were measured in single cortex cell files, starting at the cortex/endodermis initials. Cell lengths of consecutive cells were mapped as a function of cell number from the quiescent centre (QC). The fitted lines were generated with Local Polynomial Regression Fitting with the 'loess' method in R; grey shading designates the 95 percent confidence interval. Col-0 seedlings grown in the dark with and without water stress show steep slopes (green arrows). In the *trappii* mutant the curves exhibit a minimal to no difference between the different screen conditions (magenta arrows). Scale bar is 50 µm. The sample size (n) is given in each panel as the number of cells/ number of seedlings that were analyzed (A-D). Related to Fig. S11.

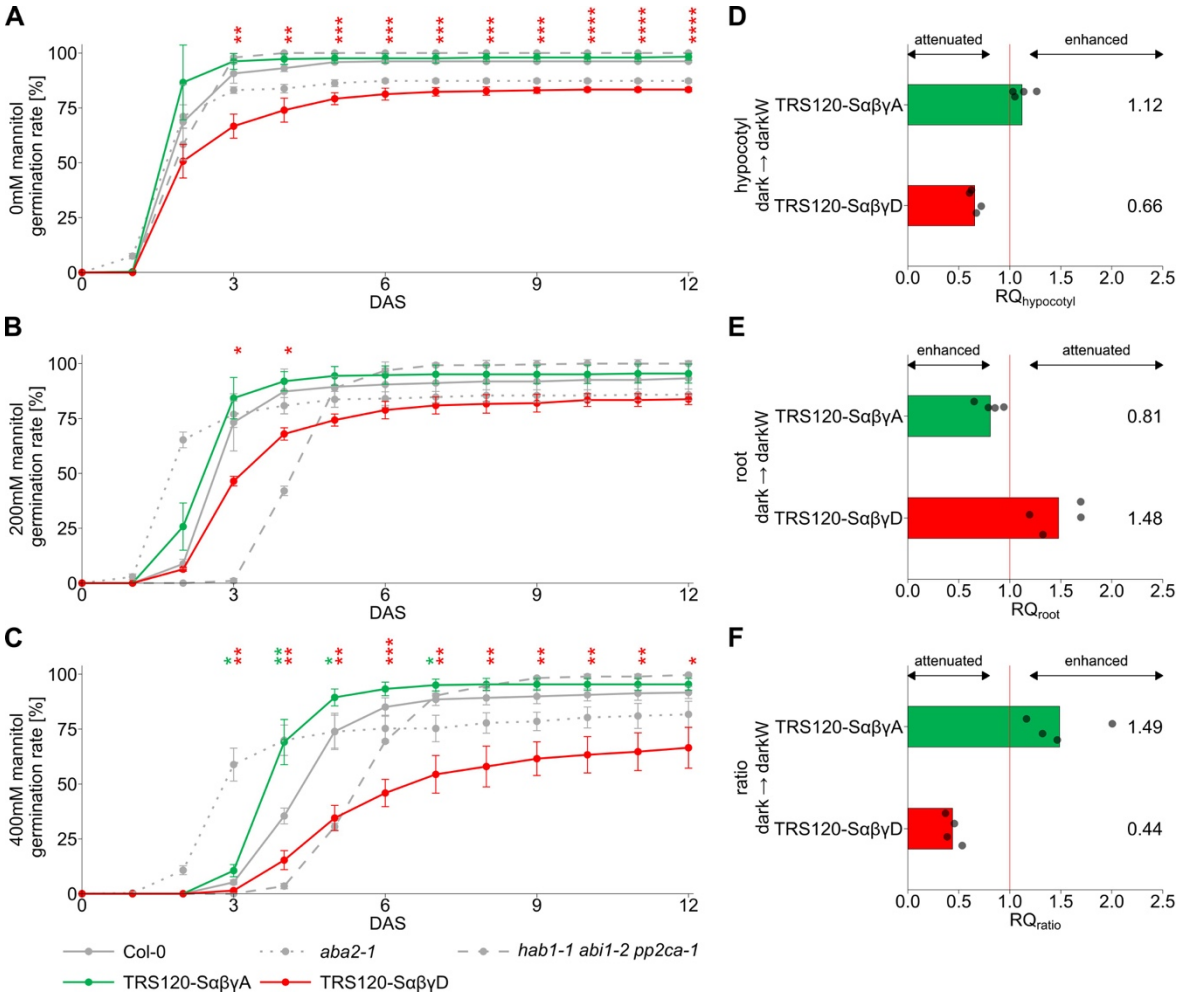


**Figure 6. Responses of TRS120 phosphovariants to osmotic or additive stress.**
Phosphovariants of $P_{TRS120}$::TRS120:GFP (Rybak *et al*, 2014) were in *trs120-4* homozygous backgrounds with the exception of the TRS120-SαβγD variant in panels A-C, which was in a hemizygous *trs120-4*/+ background.

**A-C.** Germination of TRS120 phosphovariants under osmotic stress**.** Effect of A) 0 mM, B) 200 mM and C) 400 mM mannitol on seed germination of the TRS120-SαβγA, the TRS120-SαβγD mutants and the following controls: Col-0 wild type; the ABA deficient mutant *aba2-1* and the ABA PP2C coreceptor triple knock-out line *hab1-1 abi1-2 pp2ca-1*. The non-phosphorylatable TRS120-SαβγA mutation increased seed germination on higher mannitol concentrations, whereas the phosphomimetic TRS120-SαβγD decreased seed germination. Shown are the means ± SD of three technical replicates. Similar results were obtained in three independent biological replicates. Stars indicate statistical significance compared to the wild-type Col-0 calculated with a two-tailed student's t-test (*: P<0.05; **: P<0.01; ***: P<0.001; ****: P<0.0001). DAS: days after stratification.

**D-F**. Response quotients (RQ) of D) the hypocotyl, E) the root and F) the hypocotyl/root ratio of the non-phosphorylatable TRS120-SαβγA and the phosphomimetic TRS120-SαβγD mutants for dark-to-dark with water stress (-0.4 MPa, darkW) adaptation. The divergent hypocotyl and root responses of TRS120-SαβγA and TRS120-SαβγD mutants resulted in a strong hypocotyl/root ratio phenotype under darkW conditions compared to the TRS120-WT control. TRS120-SαβγA showed an enhanced ratio adaption, whereas TRS120-SαβγD mutants had an attenuated ratio response. RQ response quotients are normalized to the rescue mutant TRS120-WT ($P_{TRS120}$::TRS120:GFP in *trs120-4/trs120-4*). A value of 1 (vertical red line) corresponds to an identical adaptation to darkW conditions as the rescue mutant. Note that due to the opposite adaptations of the hypocotyl and root under the additive stress conditions (decrease in hypocotyl and increase in root length from dark-to-darkW), the respective thresholds for attenuated and enhanced

responses are opposite. Dots represent biological replicates, of which there were a total of four primary transformants per line. Mean RQ values are given on the right. Related to Fig. S14-S15.

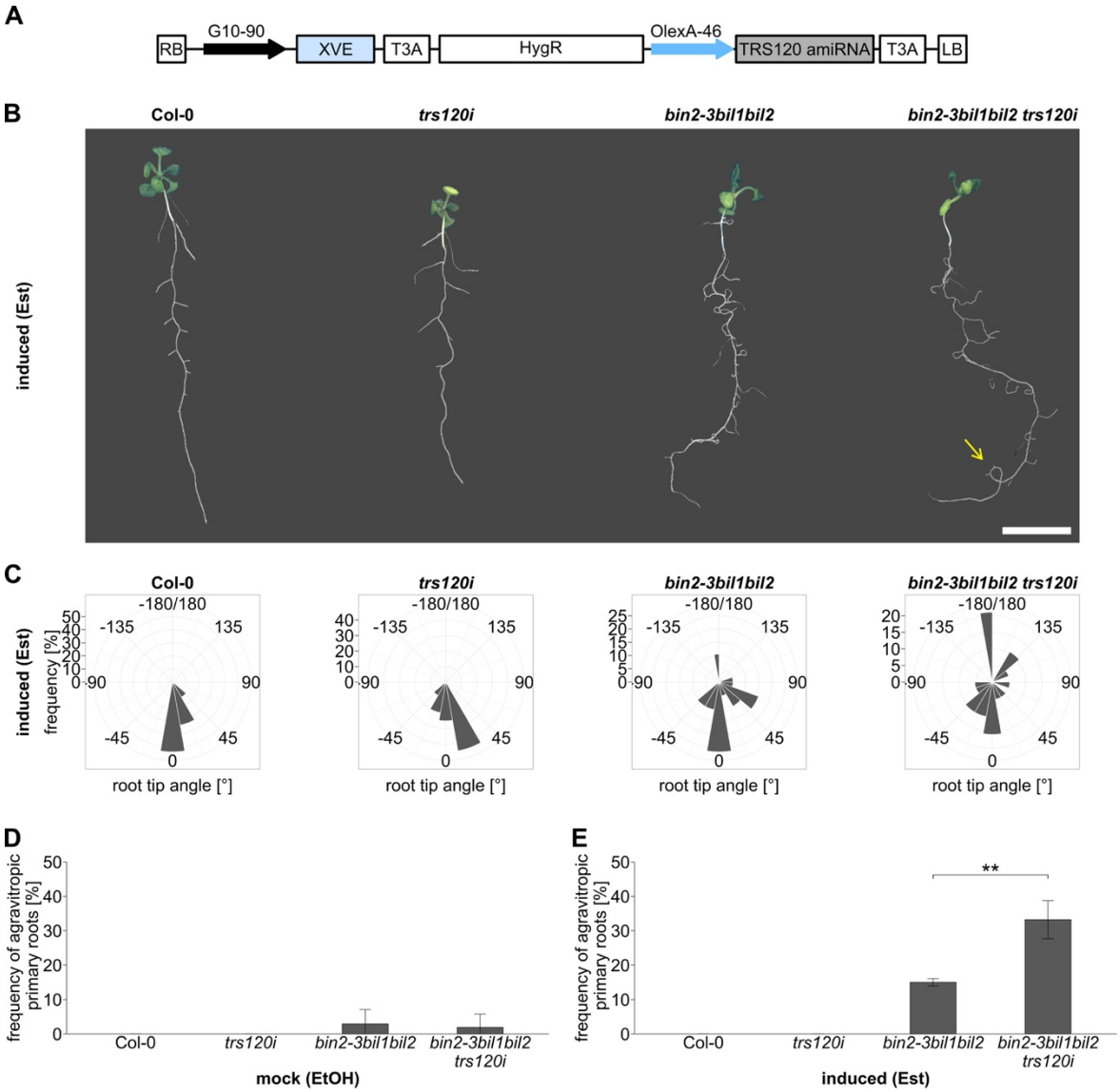


**Figure 7. Genetic interaction between *bin2* higher order and *trappii* conditional mutants**

Seedlings were transferred to estradiol (Est; induced) or EtOH (mock) containing media and grown vertically for 9 days.

**A.** A conditional *trs120* knock-down allele, *trs120i*. This features an artificial microRNA targeting the 5' end of the AtTRS120/TRAPPC9 coding sequence, expressed under an estradiol-inducible promoter. LB: left border; RB: right border; G10-90: synthetic constitutive promoter; XVE: encoding a chimeric transcription factor composed of the DNA-binding domain of the bacterial repressor LexA (X), the acidic transactivating domain of VP16 (V) and the regulatory region of the human estrogen receptor (E); T3A: poly(A) addition sequence; HygR: hygromycin resistance marker; OlexA-46: estradiol inducible promoter system with multiple copies of the lexA binding domain.

**B.** Representative seedling images of Col-0 (wild type), *trs120i* mutant, *bin2-3bil1bil2* and *bin2-3bil1bil2 trs120i* higher order mutants grown on estradiol. Upon induction, *trs120i* exhibited a mild phenotype, with a wavy primary root, and *bin2-3bil1bil2* a more pronounced root agravitropism. In contrast, *bin2-3bil1bil2 trs120i* mutants had an enhanced root agravitropism, growing against gravity or in loops (yellow arrow points to a 360° loop in the primary root). Scale bar is 1 cm.

**C.** Visualisation of the primary root growth orientation. Primary root tip angles (excluding lateral roots) of Col-0, *trs120i*, *bin2-3bil1bil2* and *bin2-3bil1bil2 trs120i* seedlings grown on Est were measured and a frequency count with a bin width of 20° was performed. Frequency plots were generated by using a polar coordinate system. A root tip angle of 0° corresponds to vertical root tip growth in line with the gravitropic

vector. Primary roots exhibiting looping (see yellow arrow in B) were scored as -180° due to their growth against gravity. A representative plot for each genotype is shown.

**D, E.** Quantification of the frequency of agravitropic primary roots upon growth on D) mock (EtOH) or E) induced (Est) conditions. Frequency of primary root tips growing against gravity (angles < -90° and > 90° in panel C) was counted per experiment. The *bin2-3bil1bil2 trs120i* higher order mutant had a more than additively enhanced agravitropic response upon induction as compared to *trs120i* or *bin2-3bil1bil2* alone (E). Note the synthetic enhancement specifically upon estradiol induction and not in the mock control (Fig. 7D, compared to 7E). This is indicative of a synergistic genetic interaction. Mean ± SD bar graphs; **: P≤0.01 two-tailed student's t-test. n = 2 independent experiments for Col-0 and *bin2-3bil1bil2*, n = 4 for *bin2-3bil1bil2 trs120i* and n = 6 for *trs120i* with at least 11 seedlings per experiment.

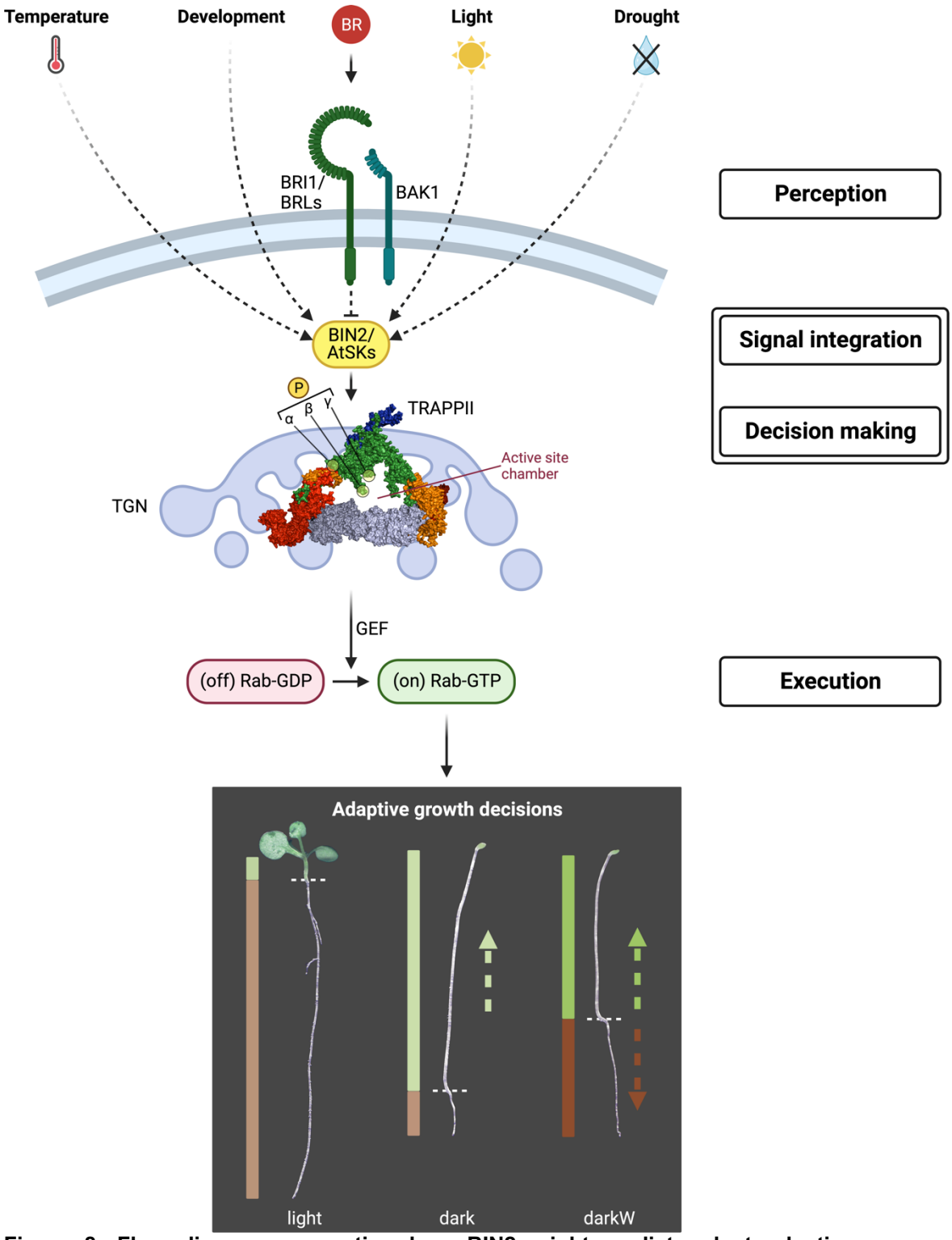


**Figure 8. Flow diagram suggesting how BIN2 might mediate plant adaptive responses by phosphorylating the TRAPPII complex.**
Shaggy-like kinases such as BIN2 integrate a vast number of signaling pathways and, together with receptor complexes at the cell surface, comprise a surveillance system fine-tuned to both biotic and abiotic cues (see text for further detail). BIN2 resides at the plasma membrane (PM) and in the cytosol and TRAPPII resides at the cytosol and in the TGN (Vert & Chory, 2006; Qi *et al*, 2011; Naramoto *et al*, 2014; Rybak *et al*, 2014;

Ravikumar *et al*, 2018). We propose that, in the cytosol, the BIN2-TRAPPII interaction serves in the relay of information from the PM to the TGN. We posit that signal integration and decision-making occur at the AtSK-TRAPPII interface. A surface view of the AtTRAPPII complex with AtTRS120 GSK3 phosphorylation sites facing the predicted active site chamber is depicted as AlphaFold structures of AtTRS120/TRAPPC9 and CLUB/AtTRS130/TRAPPC10 mapped onto the cryo-EM-generated structures of yeast TRAPPII (Mi *et al*, 2022; see Fig. S4 for a cross-kingdom structural alignment). Downstream of TRAPPII, Rab GTPase cascades are postulated to be implicated in implementing decisions reached by the AtSK-TRAPPII module. We speculate that the phosphorylation status of AtTRS120 modulates the specificity of the putative TRAPPPII GEF activity, thereby differentially activating distinct Rab GTPase cascades.
In the lower panel, we show one example of an adaptive growth decision in 10-day-old seedlings (Col-0 wild type). Bar plots depict hypocotyl (green) versus root (beige-brown) lengths. Light: light-grown seedling with a short hypocotyl and a long root. Dark: a seedling germinated in the dark with a long hypocotyl and a short root. DarkW: Water deprivation in the dark; the hypocotyl is shorter and the root longer than under dark conditions. The dotted green arrow (dark, darkW) represents the incentive for hypocotyl elongation in search of light and the brown arrow (darkW) the incentive for root growth in search of water. Thus, darkW is a “conflict of interest” scenario in which hypocotyl and root growth have competing interests (Kalbfuß *et al*, 2022). Figure generated with BioRender.